The desingularized point vortices : analysis of numerical convergence and application to a jet flow

Opleiding
Wiskunde voor de Industrie
Eindhoven

STUDENT REPORT 95 - 05

THE DESINGULARIZED POINT VORTICES: ANALYSIS OF NUMERICAL CONVERGENCE AND APPLICATION TO A JET FLOW

Seydou Fadoulourahmane

January 1995

THE DESINGULARIZED POINT VORTICES: ANALYSIS OF NUMERICAL CONVERGENCE AND APPLICATION TO A JET FLOW

SEYDOU FADOULOURAHMANE

ECMI Project
Laboratory of Fluid Mechanics and Heat Transfer
Eindhoven University of Technology
The Netherlands

coaches: Dr. S.W. Rienstra
Ir. G. Hofmans

ABSTRACT. In the year 1931 Rosenhead was the first to calculate the vortex sheet roll-up by use of point vortices as an approximation method. Later more refined calculations indicated that this method leads to chaotic behavior rather than the expected roll-up. Here we discuss the Krasny and Beale-Majda desingularized point vortex methods and prove numerically their convergence for an infinitely long periodic vortex sheet. Then we shall use these methods to simulate an impulsively starting flow from a slit.

In this report, I shall present a research that I have carried out between July 1994 and January 1995 at the Laboratory of Fluid Mechanics and Heat Transfer. Not before having some basic knowledge of Fluid Mechanics and a little experience with numerical computations with use of computers, I began to understand what the project was about.

In order to make the link between the industrial sense of the problem and the mathematical sense I have been kindly helped by Dr. S.W. Rienstra. Concerning the numerics and the Fluid mechanical background as well as experiments and the use of computers, I am very grateful to Ir. G. Hofmans for his very kind help. These two persons were not only the brain behind the basic ideas, but they were also dedicated researchers with a catching enthusiasm and very sympathetic coaches.

The Laboratory was a pleasant environment to work in. I would like to give special thanks to its responsible Dr.ir. A. Hirschberg for his generosity and sympathy.

The work has been supported on the one hand by the N.V. Gasunie, and on the other hand by the COMETT grant and a financial aid from my Ph.D. advisor Prof. Lassi Paivarinta.

Contents

1. INTRODUCTION

In this report we shall consider a two-dimensional inviscid impulsively starting flow model for representing the flow in a domain bounded on the left by a wall and on the right by a circular boundary. The flow is assumed to separate at corners.

In this type of flow field a vorticity containing layer separates from the solid body forming a free shear layer. This shear layer will be an important part of the following pages. We shall study the infinitely thin form of it, i.e, the vortex sheet.

The study of the motion of vortex sheets in two-dimensional spaces is of great importance in many types of fluid flow problems. It belongs to the larger field of vortex dynamics, one of the main approaches to understanding fluid turbulence. To make progress in the analysis of this type of flows one may consider simpler models in which various physical effects are assumed small. Therefore we shall assume for our problem the flow of an incompressible, irrotational and inviscid fluid. In this case we shall face a potential flow problem for which the governing equations are relatively simple (both the velocity potential and the stream function satisfy the Laplace equation). However it should be pointed out that the nature of the boundary conditions and the shape of the flow domain could bring the mathematical problem into the most difficult ones arising in fluid dynamics where analytical solutions –if they exist at all– are hard to obtain.

Our plan for studying this problem is divided into three parts as follows. In the first part we recall some definitions and basic equations that we shall be using in the next two chapters. The second part will be devoted to vortex methods for describing the behavior of the vortex sheet and for studying regions of concentrated vorticity embedded in the irrotational fluid. These methods offer a physically natural intuitively appealing means for simulating incompressible fluid flow at high Reynolds numbers. The first method we shall discuss is the use of a system of point vortices as a computational model for fluid flow. This method known as Rosenhead point approximation method goes back to 1931 with the work of Rosenhead who calculated the roll-up of a vortex sheet. Later more refined calculations indicated that this method could lead to chaotic behavior rather than the expected roll-up of the vortex sheet. After the Rosenhead method we shall discuss the methods of Krasny and Beale-Majda in which the roll-up was restored by replacing the point vortices by vortices with finite cores or "blobs" of vorticity. These methods are also called "blob-methods". Finally in the third part we shall use the blob methods of the second part of the report to model the problem described at the beginning, i.e, the impulsively starting flow from a slit.

2. Preliminary equations

This section is devoted to the basic equations, that we shall refer to, related to tl properties of a fluid. A first law that holds is the conservation of mass. That is

$$\frac{\partial \rho}{\partial t} = -\nabla \cdot (\rho V)$$

where V is velocity of the fluid, ρ the density of the fluid and t is time. If we assum further that the flow is incompressible (ρ = constant) we get

$$\nabla \cdot V = 0 \tag{2.1}$$

Another equation that holds is that of conservation of momentum

$$\frac{\partial V}{\partial t} + (V \cdot \nabla) \cdot V = -\frac{1}{\rho}\nabla p + \nu \nabla^2 V + g \tag{2.2}$$

in which ρ is the density, p the velocity the pressure, ν the kinematic viscosity, g th gravitational acceleration and t is time. The velocity $V(r,t)$ depends on time and space The third equation is is the state equation

$$p = p(\rho).$$

One of the most important concept that we shall use in what follows is that of vorticity The vorticity ω is defined as the rotation of the velocity, that is

$$\omega = \nabla \times V \tag{2.3).}$$

If the vorticity is zero then the fluid motion is called **irrotational**.

Equation (2.3) shows that the vorticity is determined whenever the velocity is known The other way around is also valid. When the vorticity is known then the velocity i obtained by the Biot-Savart formula

$$V(X) = -\frac{1}{4\pi}\int_{\text{Vol}} \frac{S \times \omega(X')}{s^3}\, d\mathbf{V}(X') + V_1$$

where $s = |S|$, $S = X - X'$ and V_1 is the irrotational part of the velocity. Related to th concept of vorticity is that of circulation. The circulation Γ around a closed contour C i defined as the line integral of the tangential velocity

$$\Gamma = \int_C u \cdot ds.$$

where ds is a line element of the contour.

In an incompressible two-dimensional flow (to which we shall confine ourselves) the motion can be described from (2.1) by

$$\frac{\partial u}{\partial x} + \frac{\partial v}{\partial y} = 0$$

which guaranties the existence of a stream function ψ such that

$$u = \frac{\partial \psi}{\partial y} \quad ; \quad v = \frac{\partial \psi}{\partial x}. \tag{2.4}$$

In the case of irrotational flow we have from (2.3)

$$\frac{\partial v}{\partial x} - \frac{\partial u}{\partial y} = 0$$

which guaranties the existence of a scalar function ϕ, called the velocity potential, such that

$$u = \frac{\partial \phi}{\partial x} \quad ; \quad v = -\frac{\partial \phi}{\partial y}. \tag{2.5}$$

Since a velocity potential exists in all irrotational flows such flows are also called **potential flows**. Comparing (2.4) and (2.5) we get

$$\frac{\partial \psi}{\partial y} = \frac{\partial \phi}{\partial x}$$

$$-\frac{\partial \psi}{\partial x} = \frac{\partial \phi}{\partial y}$$

known as the Cauchy -Riemann equations. From these equations we see that both the velocity potential and the stream function satisfy the Laplace equation

$$\nabla^2 \phi = 0 \qquad \nabla^2 \psi = 0.$$

For $z = x + iy$ a complex coordinate, if we define the analytic function $W = \phi + i\psi$, often called the velocity potential we get

$$\frac{dW}{dz} = u - iv.$$

3. THE VORTEX SHEET

This chapter is devoted to the doubly infinite long vortex sheet. The vortex sheet an asymptotic model of the parallel shear flow in which the thickness of the transitic between the two streams is small compared with a typical streamwise lengthscale. It ma be defined as a row of point vortices placed side by side and very close to each other. the vortex points all rotate clockwise, then the tangential velocity immediately above to the right, while that immediately below is to the left. Thus the vortex sheet implies discontinuity of tangential velocity. Hence for an infinitely thin vortex sheet, the norm velocity is continuous across the sheet, while the tangential velocity experiences a sudde jump.

If the vortex points are not infinitely thin, then the sheet has a finite thickness and th velocity change is spread out.

Our plan for studying the behavior of the vortex sheet is as follows. We shall firs derive the equation according to which the vortex sheet evolves. Then we shall stud the evolution of its solution with some initial data. This will bring us to the well know Kelvin-Helmholtz instability that says that the vortex sheet is unstable to all disturbance Finally we describe some desingularization methods and their stability analysis.

First let us look at the general overview of temporal instability.

Classical normal mode approach.

In the normal mode approach the basic equations are linearized about some unperturbe solution. Generally the resulting equations are time translation invariant. Hence it i suggested to look for solutions with a time dependence proportional to e^{pt}. We ask fo those values of p for which the linearized equations with appropriate boundary condition possess non trivial solutions. If there are admissible values of p with $\Re(p) > 0$ the systen of equations is said to be unstable. Otherwise it is stable.

These solutions proportional to e^{pt} are called normal modes. It is assumed (and o occasion proved) that the normal modes so obtained are complete, i.e, every solution ca be written as a linear combination of the normal modes. Then, if at some time (say t equa zero) a small perturbation is introduced, its evolution in time can be followed by means o normal modes expansion. If any of the modes has $\Re(p) > 0$, the perturbation grows an there is indeed instability in physical sense.

So, the general question of temporal stability is : Does an initial perturbation grow wit time?

3.1. THE ROTT-BIRKHOFF EQUATION

Consider a vortex sheet in the three dimensional space defined by the equation

$$f(x, y) = 0$$

where f is a smooth function, positive on one side of the surface and negative on th other side. The function f is selected so that it is nowhere zero than at the surfac considered. Otherwise it is an arbitrary function.

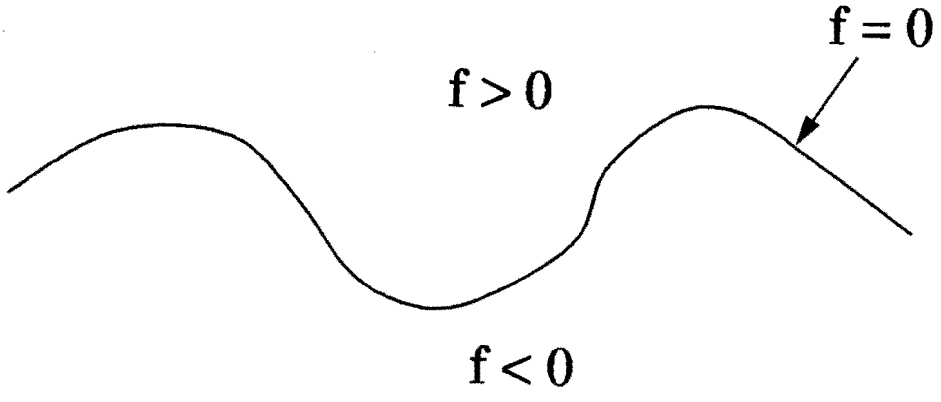

A BROAD REPRESENTATION OF THE SURFACE.

The surface $f = 0$ is filled with line-vortices in the z–direction, described by the vorticity distribution

$$\vec{\omega}(x, y, z) = \Omega(x, y)\delta(f(x, y))|\nabla f|\vec{e}_z$$

with vortex strength Ω and δ is the Dirac delta function. The factor $|\nabla f|$ is necessary for normalization; otherwise the vorticity strength becomes $f-$ dependent.

According to Biot-Savart the velocity is given by

$$\vec{v}(\vec{x}) = -\frac{1}{4\pi}\int\int\int \frac{(y-y')\vec{e}_x - (x-x')\vec{e}_y}{((x-x')^2+(y-y')^2+(z-z')^2)^{3/2}}\Omega\delta(f(x',y'))|\nabla f|\,dx'dy'dz'.$$

The integral over z is easy to calculate using

$$\int_{-\infty}^{\infty} \frac{1}{(A+(z')^2)^{3/2}}\,dz' = \frac{2}{A}.$$

Thus we obtain

$$\vec{v}(\vec{x}) = -\frac{1}{2\pi}\int\int\int \frac{(y-y')\vec{e}_x - (x-x')\vec{e}_y}{(x-x')^2+(y-y')^2}\Omega\delta(f(x',y'))|\nabla f|\,dx'dy'.$$

Now it is convenient to change to a coordinate system that moves with the surface $f = 0$. Assume

$$x = x(\gamma, \nu) \quad ; \quad y = y(\gamma, \nu)$$

so that

$$f(x(\gamma,0),y(\gamma,0))=0$$

that is $\nu=0$ corresponds to the surface.

Denote

$$x_0(\gamma)=x(\gamma,0)\quad;\quad y_0=y(\gamma,0)$$

and assume a metric such that

$$(x_0(\gamma+d\gamma)-x_0(\gamma))^2+(y_0(\gamma+d\gamma)-y_0(\gamma))^2=(d\gamma)^2\Omega^{-2}.$$

Then we get

$$(\frac{\partial x_o}{\partial\gamma})^2+(\frac{\partial y_0}{\partial\gamma})^2=\Omega^{-2}.$$

Near the surface by using the Taylor expansion and the property that $f(x_0,y_0)=0$ we get

$$\begin{aligned}f(x,y)&\approx(f(x_0(\gamma)+\nu x_\nu+\cdots,y_0(\gamma)+\nu y_\nu+\cdots\\&\approx f(x_0,y_0)+\nu(x_\nu f_x+y_\nu f_y)+\cdots\\&=\nu(x_\nu f_x+y_\nu f_y)+\cdots\end{aligned}.$$

Hence if we define

$$H(x,y)=-\frac{1}{4\pi}\frac{(y-y')\vec{e}_x-(x-x')\vec{e}_y}{(x-x')^2+(y-y')^2}\Omega|\nabla f|$$

we obtain

$$\begin{aligned}\vec{v}(\vec{x})&=\int\int H(x',y')\delta(f(x',y'))\,dx'dy'\\&=\int\int H(x',y')\delta(\nu(x_\nu f_x+y_\nu f_y))|x_\nu y_\gamma-x_\gamma y_\nu|\,d\gamma d\nu\,.\\&=\int H(x_0,y_0)|\frac{x_\nu y_\gamma-x_\gamma y_\nu}{x_\nu f_x+y_\nu f_y}|\,d\gamma\end{aligned}$$

Now let us calculate

$$|\frac{x_\nu y_\gamma-x_\gamma y_\nu}{x_\nu f_x+y_\nu f_y}|.$$

On one hand, since $f(x_0(\gamma),y_o(\gamma))$ is zero for all γ then so is its derivative with respect to γ and we get

$$x_\gamma f_x+y_\gamma f_y=0.$$

This implies that

$$x_\gamma=-y_\gamma\frac{f_y}{f_x}$$

and then

$$x_\nu y_\gamma-x_\gamma y_\nu=\frac{y_\gamma}{f_x}(x_\nu f_x+y_\nu f_y).$$

This finally yields

$$|\frac{x_\nu y_\gamma - x_\gamma y_\nu}{x_\nu f_x + y_\nu f_y}| = |\frac{y_\gamma}{f_x}|.$$

On the other hand we know that

$$(\frac{\partial x_o}{\partial \gamma})^2 + (\frac{\partial y_0}{\partial \gamma})^2 = \Omega^{-2}.$$

This implies that

$$(y_\gamma)^2 = \frac{(f_x)^2}{(f_x)^2 + (f_y)^2}\Omega^{-2}.$$

We then finally end up with

$$|\frac{x_\nu y_\gamma - x_\gamma y_\nu}{x_\nu f_x + y_\nu f_y}| = \frac{\Omega^{-1}}{|\nabla f|}.$$

Replacing this in the formula of the velocity we obtain

$$\vec{v}(\vec{x}) = -\frac{1}{2\pi}\int_{-\infty}^{\infty} \frac{(y - y_0)\vec{e}_x - (x - x_0)\vec{e}_y}{(x - x_0)^2 + (y - y_0)^2}\, d\gamma.$$

Therefore a vortex sheet, in two-dimensional ideal flow, can be described by a complex curve $z(\gamma, t) = x(\gamma, t) + iy(\gamma, t)$ where t is time and γ is a real Lagrangian variable parameterizing the sheet and measures the circulation between a base point and an arbitrary point along the sheet. If we consider an infinitely long vortex sheet then the velocity changes in time according to the momentum equation and we have that the vortex sheet evolves according to the integro differential equation

$$\frac{\partial z^*}{\partial t} = \frac{i}{2\pi}\int_{-\infty}^{\infty} \frac{d\gamma'}{z(\gamma, t) - z(\gamma', t)} \tag{3.1.a}$$

which is known as the Birkhoff-Rott equation in which the star denotes the complex conjugate. Because of the singularity at $\gamma' = \gamma$ the integral is understood as a principle value integral. The singularity at $\gamma' = \infty$ is eliminated by taking $\frac{\partial z}{\partial \gamma}$ to be periodic.

Now let us start the stability analysis for the Birkhoff-Rott equation subject to some initial shape. By analytically extending the complex conjugate, i.e, by setting

$$z^* = \bar{z}$$

we have that the contour must move with γ and we get

$$\frac{\partial \bar{z}}{\partial t} = \frac{i}{2\pi} PV \int_{-\infty}^{\infty} \frac{d\sigma}{z(\gamma, t) - z(\gamma' + \sigma, t)}. \tag{3.1.b}$$

A flat vortex sheet with uniform strength constant strength is given by

$$z = \gamma$$

which is an equilibrium solution of (3.1.a)

If we replace z by $\gamma + s$ in (3.1.b) where s is a small perturbation and neglect the terms that are quadratic in s and s' we obtain

$$\begin{aligned}\frac{\partial \bar{s}}{\partial t} &= \frac{1}{2\pi i} PV \int_{-\infty}^{\infty} \frac{s' - s}{(\gamma - \gamma')^2}\, d\gamma' \\ &= \frac{1}{2\pi} \int_{-\infty}^{\infty} \frac{s_\gamma(\gamma', t)}{\gamma' - \gamma}\, d\gamma' \\ &= \frac{1}{2} H[\partial_\gamma s][s, t]\end{aligned}$$

where $s = s(\gamma, t)$, $s' = s(\gamma', t)$, $s_\gamma = \frac{\partial s}{\partial \gamma}$ and

$$H[f][\gamma] = \frac{1}{\pi i} \int_{-\infty}^{\infty} \frac{f(\gamma + \sigma)}{\sigma}\, d\sigma$$

is the Hilbert transform that has the following property

$$H[f] = f^+ - f^-$$

where f^+ and f^- are the upper and lower analytic parts of f, respectively.

A straightforward computation gives

$$\partial_{tt} s_+ + \frac{1}{4} \partial_{\gamma\gamma} s_+ = 0.$$

If we consider $s_+ = X \exp(ik\gamma + \omega t)$ we get

$$\omega^2 = \frac{1}{4} k^2 \tag{3.1.c}$$

showing a short wave length instability or Kelvin-Helmholtz instability. Mathematically speaking the initial value problem (3.1.a) with some initial perturbation is ill–posed since a small perturbation leads to a normal mode that grows exponentially with time.

From now, for a sake of simplicity, we shall consider periodicity in the infinitely long vortex sheet as follows.

Assume the vortex sheet is periodic in γ with period 1 that is

$$z(\gamma + 1, t) = 1 + z(\gamma, t).$$

Then equation (3.1.a) becomes

$$\begin{aligned}\frac{\partial z^*}{\partial t} &= \frac{1}{2\pi i}\sum_{n=-\infty}^{\infty}\int_0^1 \frac{1}{z-\bar{z}-n}\,d\bar{\gamma} \\ &= \frac{1}{2\pi i}\int_0^1 \sum_{n=-\infty}^{\infty}\frac{1}{z-\bar{z}-n}\,d\bar{\gamma} \\ &= \frac{1}{2\pi i}\int_0^1 \cot\pi(z-\bar{z})\,d\bar{\gamma} \qquad (3.2)\end{aligned}$$

where $z = z(\gamma,t)$, $(\bar{z} = z(\bar{\gamma},t))$ and the sum is interpreted as a finite sum, i.e, $\sum_{-\infty}^{\infty} = \lim_{N\to\infty}\sum_{-N}^{N}$.

The last equality in (3.2) follows from

$$\begin{aligned}\frac{1}{\pi}\sum_{n=-\infty}^{\infty}\frac{1}{Z-n} &= \frac{1}{2\pi}\sum_{n=0}^{\infty}\left(\frac{1}{Z-n}+\frac{1}{Z+n}\right) \\ &= \frac{1}{2\pi}\sum_{n=0}^{\infty}\frac{2Z}{Z^2-n^2} \\ &= \frac{1}{\pi Z}+\frac{2Z}{\pi}\sum_{n=1}^{\infty}\frac{1}{Z^2-n^2} \\ &= \cot(\pi Z) \qquad \text{(see[GR])}.\end{aligned}$$

Using the well known identities

$$\cos z = \cos(x+iy) = \cos x\cosh y - i\sin x\sinh y$$

$$\sin z = \sin(x+iy) = \sin x\cosh y + i\cos x\sinh y$$

equation (3.2) can be transformed to the real plane and becomes

$$\frac{\partial x}{\partial t} = \frac{-1}{2}\int_0^1 \frac{\sinh 2\pi(y-\bar{y})}{\cosh 2\pi(y-\bar{y})-\cos 2\pi(x-\bar{x})}\,d\bar{\gamma} \qquad (3.3.a)$$

$$\frac{\partial y}{\partial t} = \frac{1}{2}\int_0^1 \frac{\sin 2\pi(x-\bar{x})}{\cosh 2\pi(y-\bar{y})-\cos 2\pi(x-\bar{x})}\,d\bar{\gamma} \qquad (3.3.b)$$

where the integrals are understood as principal values.

Next we shall consider the problem of finding x and y in integro-differential equation (3.3) with initial conditions

$$x(\gamma,0) = \gamma + 0.01\sin(2\pi\gamma) \qquad (3.4.a)$$

$$y(\gamma,0) = -0.01\sin(2\pi\gamma') \tag{3.4.b}$$

For the numerical integration of equations (3.3) various methods have been introduced in this century. The most standard is the following.

3.2 The point vortex approximation method

A first approach (as far as we know) to the numerical solution of problem (3.3), (3.4) is due to Rosenhead. In his approach, the curve $z(\gamma,t)$ is approximated by a finite number of points $z_j(t) \approx z(\gamma_j,t)$ corresponding to a uniform $\gamma-$ mesh. $\gamma_j = (j-1)\Delta\gamma, j = 1,\cdots,N$; $N = \frac{1}{\Delta\gamma}$ is the number of points per wave length.

The integrals in (3.3) are approximated by a quadrature rule that omits the infinite contribution due to the the integrand's singularity at $\gamma = \bar{\gamma}$.

The discretization yields

$$\frac{dx_j}{dt} = \frac{-1}{2N}\sum_{k=1,k\neq j}^{N} \frac{\sinh 2\pi(y_j - y_k)}{\cosh 2\pi(y_j - y_k) - \cos 2\pi(x_j - x_k)} \tag{3.5.a}$$

$$\frac{dy_j}{dt} = \frac{1}{2N}\sum_{k=1,k\neq j}^{N} \frac{\sin 2\pi(x_j - x_k)}{\cosh 2\pi(y_j - y_k) - \cos 2\pi(x_j - x_k)} \tag{3.5.b}$$

In this case linear stability analysis shows (see []) that problem (3.5) has solutions proportional to $\exp(2\pi(\omega t + i\frac{kj}{N}))$ when the discrete dispersion relation

$$\omega^2 = \frac{1}{4}k^2(1-\frac{k}{N})^2$$

is satisfied.

From this dispersion relation we see that, for fixed k, if N tends to infinity the relation (3.1.c) of the exact vortex sheet is recovered. This shows a consistency of the method.

However this method is far from satisfactory. First, the approximated velocity is unbounded and can not approximate a bounded velocity in any reasonable norm. Second, there exists a critical time $t_c = 0.375$ past which a singularity is forming in the vortex sheet. Third, past this critical time the vortex sheet does not converge to the expected roll-up. For more details and numerical examples we refer to [K1].

In conclusion we see that the point vortex method is just too singular to approximate the physical reality satisfactorily. We shall consider in the following two sections two methods that avoid the above mentioned difficulties.

3.3 Krasny desingularization method

The first desingularization method (using "blobs") has been introduced by Chorin and Bernard. They felt that it is the high induced velocities which occur when two vortices come close together that invalidates the model and suggested the introduction of core of

point vortices to the vortices. The equation of the Biot-Savart kernel for a single vortex becomes

$$K_\delta = K(z) \quad \text{for} \quad |z| > \delta$$

$$K_\delta = K(z)\frac{|z|}{\delta} \quad \text{for} \quad |z| \leq \delta$$

where δ is a small cut-off distance and

$$K(z) = \frac{i}{2\pi}\frac{1}{z}.$$

Inspired by this method Krasny [K2] developed the following method. The Krasny desingularization method consists of considering the approximated kernel

$$K_\delta(z-\bar{z}) = \frac{\cos\pi(z-\bar{z})}{|\sin\pi(z-\bar{z})|^2+\delta^2}\sin\pi(z-\bar{z})^*$$

instead of

$$K(z-\bar{z}) = \frac{\cos\pi(z-\bar{z})}{\sin\pi(z-\bar{z})}$$

the kernel in (3.2).

Obviously, $K_\delta \to K$ as $\delta \to 0$. In this case the problem to be studied is

$$\frac{\partial x}{\partial t} = \frac{-1}{2}\int_0^1 \frac{\sinh 2\pi(y-\bar{y})}{\cosh 2\pi(y-\bar{y}) - \cos 2\pi(x-\bar{x}) + \delta^2}\, d\bar{\gamma} \tag{3.6.a}$$

$$\frac{\partial y}{\partial t} = \frac{1}{2}\int_0^1 \frac{\sin 2\pi(x-\bar{x})}{\cosh 2\pi(y-\bar{y}) - \cos 2\pi(x-\bar{x}) + \delta^2}\, d\bar{\gamma} \tag{3.6.b}$$

with initial conditions

$$x(\gamma,0) = \gamma + 0.01\sin 2\pi\gamma \quad y(\gamma,0) = -0.01\sin 2\pi\gamma. \tag{3.7}$$

This method is also called Krasny blob method since it uses "blobs" to desingularize the integrand. In a free space one takes

$$K_\delta(z) = K(z)\frac{|z|^2}{|z|^2+\delta^2} \tag{3.8}$$

for one point vortex.

Linear Stability Analysis.

As in last sections we consider the flat, constant vortex sheet with small perturbations

$$x(\gamma,t)=\gamma+x'(\gamma,t)\qquad y(\gamma,t)=y'(\gamma,t).$$

Replacing these equations into the integrodifferential equations (3.6) neglecting the terms that are quadratic in x' and y' we get

$$\begin{aligned}\frac{\partial x'}{\partial t}&=-\pi\int_0^1\frac{(y'-\bar{y}')}{1-\cos 2\pi(\gamma-\bar{\gamma})+\sin 2\pi(\gamma-\bar{\gamma})2\pi(x'-\bar{x}')+\delta^2}\,d\bar{\gamma}\\&=-\pi\int_0^1\frac{(y'-\bar{y}')}{(1-\cos 2\pi(\gamma-\bar{\gamma})+\delta^2)(1+\frac{\sin 2\pi(\gamma-\bar{\gamma})2\pi(x'-\bar{x}')}{1-\cos 2\pi(\gamma-\bar{\gamma})+\delta^2})}\,d\bar{\gamma}\\&\approx-\pi\int_0^1\frac{(y'-\bar{y}')}{(1-\cos 2\pi(\gamma-\bar{\gamma})+\delta^2)}(1-\frac{\sin 2\pi(\gamma-\bar{\gamma})2\pi(x'-\bar{x}')}{1-\cos 2\pi(\gamma-\bar{\gamma})+\delta^2})\,d\bar{\gamma}\\&\approx-\pi\int_0^1\frac{(y'-\bar{y}')}{(1-\cos 2\pi(\gamma-\bar{\gamma})+\delta^2)}\,d\bar{\gamma}\end{aligned}$$

Similarly

$$\begin{aligned}\frac{\partial y'}{\partial t}&=\frac{1}{2}\int_0^1\frac{2\pi(x'-\bar{x}')\cos 2\pi(\gamma-\bar{\gamma})+\sin 2\pi(\gamma-\bar{\gamma})}{(1-\cos 2\pi(\gamma-\bar{\gamma})+\delta^2)}(1-\frac{\sin 2\pi(\gamma-\bar{\gamma})2\pi(x'-\bar{x}')}{1-\cos 2\pi(\gamma-\bar{\gamma})+\delta^2})\,d\bar{\gamma}\\&\approx-\pi\int_0^1\frac{(x'-\bar{x}')(1-(1+\delta^2)\cos 2\pi(\gamma-\bar{\gamma}))}{(1-\cos 2\pi(\gamma-\bar{\gamma})+\delta^2)^2}\,d\bar{\gamma}\end{aligned}$$

Hence we obtain

$$\begin{aligned}\frac{\partial x'}{\partial t}&=-\pi\int_0^1\frac{(y'-\bar{y}')}{(1-\cos 2\pi(\gamma-\bar{\gamma})+\delta^2)}\,d\bar{\gamma}\\\frac{\partial y'}{\partial t}&=-\pi\int_0^1\frac{(x'-\bar{x}')(1-(1+\delta^2)\cos 2\pi(\gamma-\bar{\gamma}))}{(1-\cos 2\pi(\gamma-\bar{\gamma})+\delta^2)^2}\,d\bar{\gamma}.\end{aligned}$$

If we replace x' and y' in the last two equations by $Xe^{2\pi(\omega t+ik\gamma)}$ and $Ye^{2\pi(\omega t+ik\gamma)}$, respectively we get

$$2\omega X=-Y\int_0^1\frac{1-e^{2\pi ik\gamma}}{(1-\cos 2\pi\gamma+\delta^2)}\,d\gamma$$

and

$$2\omega Y=-X\int_0^1\frac{(1-e^{2\pi ik\gamma})(1-(1+\delta^2)\cos 2\pi\gamma)}{(1-\cos 2\pi\gamma+\delta^2)^2}\,d\gamma$$

yielding

$$\omega^2=\frac{1}{4}\int_0^1\frac{1-e^{2\pi ik\gamma}}{(1-\cos 2\pi(\gamma)+\delta^2)}\,d\gamma\times\int_0^1\frac{(1-e^{2\pi ik\gamma})(1-(1+\delta^2)\cos 2\pi\gamma}{(1-\cos 2\pi\gamma+\delta^2)^2}\,d\gamma.$$

The two integrals in this last expression my be evaluated by the residue theorem as follows.

First consider

$$I_1 = \int_0^1 \frac{1 - e^{2\pi i k\gamma}}{(1 - \cos 2\pi\gamma + \delta^2)}\, d\gamma.$$

Take

$$e^{2\pi i\gamma} = z$$

we get

$$I_1 = 2\pi i \int_{|z|=1} \frac{1 - z^k}{z^2 - 2(1+\delta^2)z + 1}\, dz.$$

The denominator of the integrand is zero for z equal to z_1 and z_2 such that

$$z_1 = 1 + \delta^2 - \delta\sqrt{2+\delta^2} \quad \text{and} \quad z_2 = 1 + \delta^2 + \delta\sqrt{2+\delta^2}.$$

For $\delta > 0$ the only singularity of the integrand on the unit disc is at $z = z_1$. Furthermore; it is a pole of first order, so the residue of the integrand is

$$\lim_{z \to z_1} 2\pi i \frac{1 - z^k}{z - z_2}.$$

Since (see [Gr])

$$\log(1 + \delta^2 - \delta\sqrt{2+\delta^2}) = -\operatorname{arcosh}(1+\delta^2) \tag{3.9}$$

we get by the residue theorem

$$I_1 = \frac{1 - z_1^k}{z_1 - z_2} = \frac{1 - e^{-k \operatorname{arcosh}(1+\delta^2)}}{\delta\sqrt{2+\delta^2}}.$$

In a similar way using the same change of variable as before we get for

$$I_2 = \int_0^1 \frac{(1 - e^{2\pi i k\gamma})(1 - (1+\delta^2)\cos 2\pi\gamma}{(1 - \cos 2\pi\gamma + \delta^2)^2}\, d\gamma$$

the dispersion in z

$$I_2 = 2\pi i \int_{|z|=1} \frac{(1 - z^k)(1 - (1+\delta^2)(z^{-1} + z))}{(z^2 - 2(1+\delta^2)z + 1)^2}\, dz.$$

Therefore the integrand of I_2 has the same singularity as I_1 but a pole of second order. The residue of the integrand is

$$\lim_{z \to z_1} \left(2\pi i \frac{(1 - z^k)(1 - (1+\delta^2)(z^{-1} + z))}{(z^2 - 2(1+\delta^2)z + 1)^2}\right)'.$$

Using (3.9) the residue theorem yields

$$I_2 = k\, e^{-k\,\mathrm{arcosh}(1+\delta^2)}.$$

Finally we obtain

$$\omega^2 = \frac{1}{4}\frac{1 - e^{-k\ \mathrm{arcosh}(1+\delta^2)}}{\delta\sqrt{2+\delta^2}}\, k\, e^{-k\,\mathrm{arcosh}(1+\delta^2)}$$

from which we readily see that for fixed k

$$\lim_{\delta\to 0} \omega^2 = \frac{k^2}{4}$$

which is the dispersion relation of the real solution($\delta = 0$) (3.1.c).

On the other hand we also see that

$$\lim_{k\to\infty} \omega(k) = 0$$

showing that the short wavelength instability that occurs for the vortex sheet and the point vortex method has been considerably reduced.

In fig. 3.1. we represent the relation $\omega(k)$ for different values of δ.

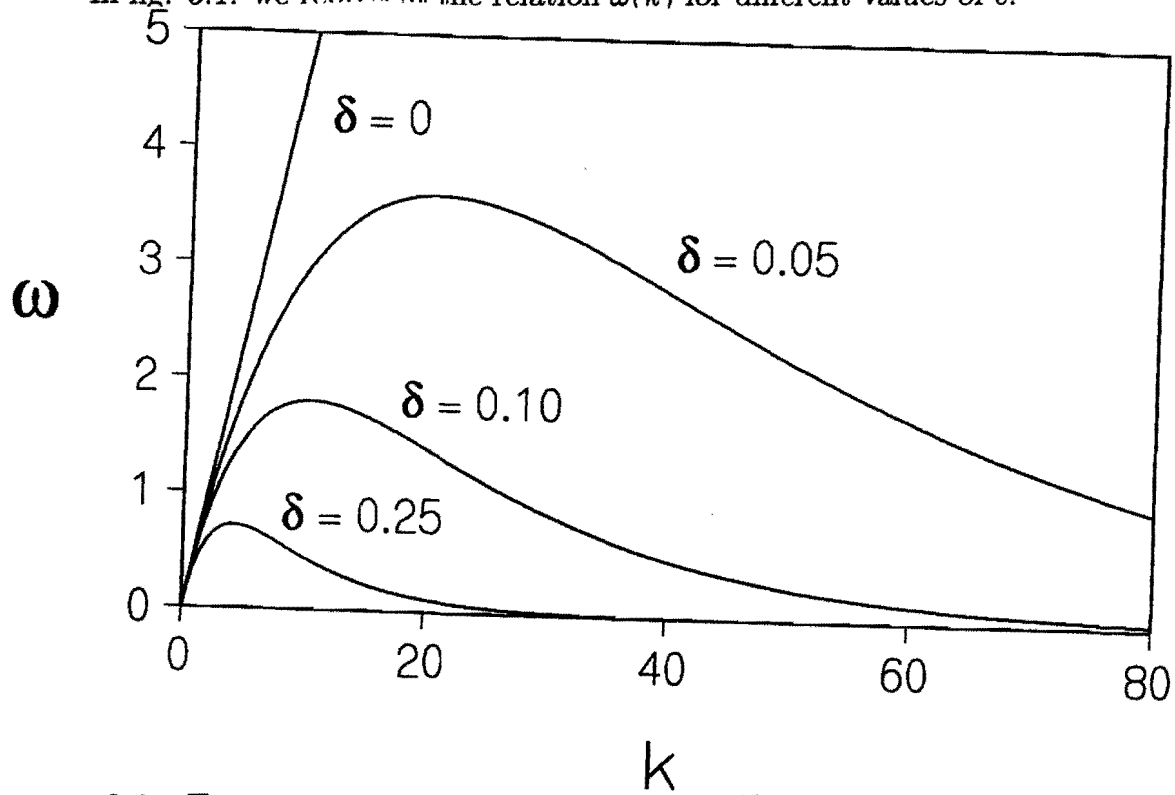

FIG. 3.1. THE LINEAR DISPERSION RELATION $\omega(k)$ OF THE DESINGULARIZED EQUATIONS USING THE KRASNY METHOD FOR DIFFERENT VALUES OF δ. THE STRAIGHT LINE IS THE DISPERSION RELATION OF KELVIN-HELMHOLTZ INSTABILITY ($\delta = 0$).

3.4 Beale-Majda desingularization method

Here we have been motivated by the Beale and Majda method in [BM] where they considered in a free space a desingularized kernel

$$K_\delta(z) = K(z)(1 - e^{-|z|^2/\delta^2})$$

and the Krasny desingularization method for the periodic vortex sheet discussed in the previous section. We desingularize the vortex sheet at the endpoints as well as at their neighboring points and the desingularization method consists of considering the approximated kernel

$$K_\delta = \frac{\cos \pi(z - \bar{z})}{\sin \pi(z - \bar{z})} f_\delta(x - \bar{x}, y - \bar{y}) \tag{3.10}$$

where

$$f_\delta(x - \bar{x}, y - \bar{y}) = \prod_{j=-\infty}^{\infty} (1 - e^{-\frac{(x-\bar{x}-j)^2+(y-\bar{y})^2}{\delta^2}}),$$

$$z = x + iy \qquad \bar{z} = \bar{x} + i\bar{y}$$

instead of

$$K = \frac{\cos \pi(z - \bar{z})}{\sin \pi(z - \bar{z})}$$

the kernel of the integral in (3.2). Here also, $K_\delta \to K$ as $\delta \to 0$ and he problem to study is

$$\frac{\partial x}{\partial t} = \frac{-1}{2} \int_0^1 \frac{\sinh 2\pi(y - \bar{y}) f_\delta}{\cosh 2\pi(y - \bar{y}) - \cos 2\pi(x - \bar{x})} \, d\bar{\gamma} \tag{3.11.a}$$

$$\frac{\partial y}{\partial t} = \frac{1}{2} \int_0^1 \frac{\sin 2\pi(x - \bar{x}) f_\delta}{\cosh 2\pi(y - \bar{y}) - \cos 2\pi(x - \bar{x})} \, d\bar{\gamma} \tag{3.11.b}$$

with initial conditions

$$x(\gamma, t) = \gamma + 0.01 \sin 2\pi\gamma$$

$$y(\gamma, t) = -0.01 \sin 2\pi\gamma$$

where x and $\bar{x}$ are as in the last sections.

Linear Stability Analysis.

As in last sections we consider the flat, constant vortex sheet with small perturbations

$$x(\gamma,t) = \gamma + x'(\gamma,t) \qquad y(\gamma,t) = y'(\gamma,t).)$$

Replacing these equations into the integrodifferential equations (3.11) extending the denominator and f_δ neglecting the terms that are quadratic in x' and y' we get for f_δ the expression

$$I_\delta = F_\delta|_{x-\bar{x}=y-\bar{y}=0} + (x-\bar{x})\frac{\partial F_\delta}{\partial(x-\bar{x})}|_{x-\bar{x}=y-\bar{y}=0} + (y-\bar{y})\frac{\partial F_\delta}{\partial(y-\bar{y})}|_{x-\bar{x}=y-\bar{y}=0}$$

where

$$F_\delta := f_\delta(x'-\bar{x}'+\gamma-\bar{\gamma}, y'-\bar{y}')$$

and equations (3.11) become

$$\begin{aligned}
\frac{\partial x'}{\partial t} &= -\pi\int_0^1 \frac{(y'-\bar{y}')F_\delta|_{x'-\bar{x}'=y'-\bar{y}'=0}}{1-\cos 2\pi(\gamma-\bar{\gamma})+\sin 2\pi(\gamma-\bar{\gamma})2\pi(x'-\bar{x}')}\,d\bar{\gamma} \\
&= -\pi\int_0^1 \frac{(y'-\bar{y}')F_\delta|_{x'-\bar{x}'=y'-\bar{y}'=0}}{(1-\cos 2\pi(\gamma-\bar{\gamma}))(1+\frac{\sin 2\pi(\gamma-\bar{\gamma})2\pi(x'-\bar{x}')}{1-\cos 2\pi(\gamma-\bar{\gamma})}}\,d\bar{\gamma} \\
&= -\pi\int_0^1 \frac{(y'-\bar{y}')F_\delta|_{x'-\bar{x}'=y'-\bar{y}'=o}}{(1-\cos 2\pi(\gamma-\bar{\gamma}))}(1-\frac{\sin 2\pi(\gamma-\bar{\gamma})2\pi(x'-\bar{x}')}{1-\cos 2\pi(\gamma-\bar{\gamma})}\,d\bar{\gamma} \\
&= -\pi\int_0^1 \frac{(y'-\bar{y}')F_\delta|_{x'-\bar{x}'=y'-\bar{y}'=0}}{(1-\cos 2\pi(\gamma-\bar{\gamma}))}\,d\bar{\gamma}.
\end{aligned}$$

Similarly

$$\begin{aligned}
\frac{\partial y'}{\partial t} &= \frac{-1}{2}\int_0^1 \frac{2\pi(x'-\bar{x}')\cos 2\pi(\gamma-\bar{\gamma})+\sin 2\pi(\gamma-\bar{\gamma})}{(1-\cos 2\pi(\gamma-\bar{\gamma}))} \\
&\quad\times(1-\frac{\sin 2\pi(\gamma-\bar{\gamma})2\pi(x'-\bar{x}')}{1-\cos 2\pi(\gamma-\bar{\gamma})}I_\delta\,d\bar{\gamma} \\
&= -\pi\int_0^1 \frac{(x'-\bar{x}')(\cos 2\pi(\gamma-\bar{\gamma})F_\delta|_{x'-\bar{x}'=y'-\bar{y}'-0}+\frac{\sin 2\pi(\gamma-\bar{\gamma})}{2\pi}G_\delta)}{1-\cos 2\pi(\gamma-\bar{\gamma})}\,d\bar{\gamma}
\end{aligned}$$

where

$$G_\delta = \frac{\partial F_\delta}{\partial(x'-\bar{x}')}|_{x'-\bar{x}'=y'-\bar{y}'=0}.$$

Hence we obtain

$$\begin{aligned}
\frac{\partial x'}{\partial t} &= -\pi\int_0^1 \frac{(y'-\bar{y}')F_\delta|_{x'-\bar{x}'=y'-\bar{y}'=0}}{(1-\cos 2\pi(\gamma-\bar{\gamma}))}\,d\bar{\gamma} \\
\frac{\partial y'}{\partial t} &= -\pi\int_0^1 \frac{(x'-\bar{x}')(\cos 2\pi(\gamma-\bar{\gamma})F_\delta|_{x'-\bar{x}'=y'-\bar{y}'=0}+\frac{\sin 2\pi(\gamma-\bar{\gamma})}{2\pi}G_\delta)}{1-\cos 2\pi(\gamma-\bar{\gamma})}\,d\bar{\gamma}.
\end{aligned}$$

If we replace x' and y' in the last two equations by $Xe^{2\pi(wt+ik\gamma)}$ and $Ye^{2\pi(wt+ik\gamma)}$, respectively we get

$$2wX = -Y \int_0^1 \frac{1 - e^{2\pi ik\gamma} F_\delta}{(1 - \cos 2\pi\gamma)} \, d\gamma$$

and

$$2wY = -X \int_0^1 \frac{(1 - e^{2\pi ik\gamma})(\cos 2\pi\gamma F_\delta|_{x'-\bar{x}'=y'-\bar{y}'-0} + \frac{\sin 2\pi\gamma}{2\pi} \frac{\partial F_\delta}{\partial(x'-\bar{x}')}|_{x'-\bar{x}'=y'-\bar{y}'=0})}{1 - \cos 2\pi\gamma} \, d\gamma.$$

yielding

$$\omega^2 = J_1 \times J_2$$

where

$$J_1 = \frac{1}{4} \int_0^1 \frac{(1 - e^{2\pi ik\gamma}) F_\delta}{(1 - \cos 2\pi\gamma)} \, d\gamma$$

and

$$J_2 = \int_0^1 \frac{(1 - e^{2\pi ik\gamma})(\cos 2\pi\gamma F_\delta|_{x'-\bar{x}'=y'-\bar{y}'-0} + \frac{\sin 2\pi\gamma}{2\pi} \frac{\partial F_\delta}{\partial(x'-\bar{x}')}|_{x'-\bar{x}'=y'-\bar{y}'=0})}{1 - \cos 2\pi\gamma} \, d\gamma.$$

the dispersion relation of $\omega(k)$ for different values of δ is plotted in fig. (3.2).

As in the case of Krasny method we see from fig. 3.2. that there exists a maximum value k_m of wave number for which $\omega(k_m)$ is maximum and when k tends to infinity w tends to zero.

3.5 Numerical results for vortex methods

The technique of discretization to solve the initial value problems (3.6) and (3.11) with initial conditions (3.7) is as in the point vortex method.

For $0 \leq \gamma \leq 1$ the curve $(x(\gamma,t), y(\gamma,t))$ is approximated by a finite number of points $((x_j(t), y_j(t)) \approx (x(\gamma_j,t), y(\gamma_j,t))$ corresponding of a uniform $\gamma-$ mesh,

$$\gamma_j = (j-1)\Delta\gamma, \qquad j = 1, \cdots, N \qquad \Delta\gamma = \frac{1}{N}.$$

Trapezoidal quadrature yields a system of ordinary differential equations for the points trajectories. for equations (3.6) we have

$$(3.12.a) \qquad \frac{dx_j}{dt} = \frac{-1}{2N} \sum_{k=1,k\neq j}^{N} \frac{\sinh 2\pi(y_j - y_k)}{\cosh 2\pi(y_j - y_k) - \cos 2\pi(x_j - x_k) + \delta^2}$$

$$(3.12.a) \qquad \frac{dy_j}{dt} = \frac{1}{2N} \sum_{k=1,k\neq j}^{N} \frac{\sin 2\pi(x_j - x_k)}{\cosh 2\pi(y_j - y_k) - \cos 2\pi(x_j - x_k) + \delta^2}$$

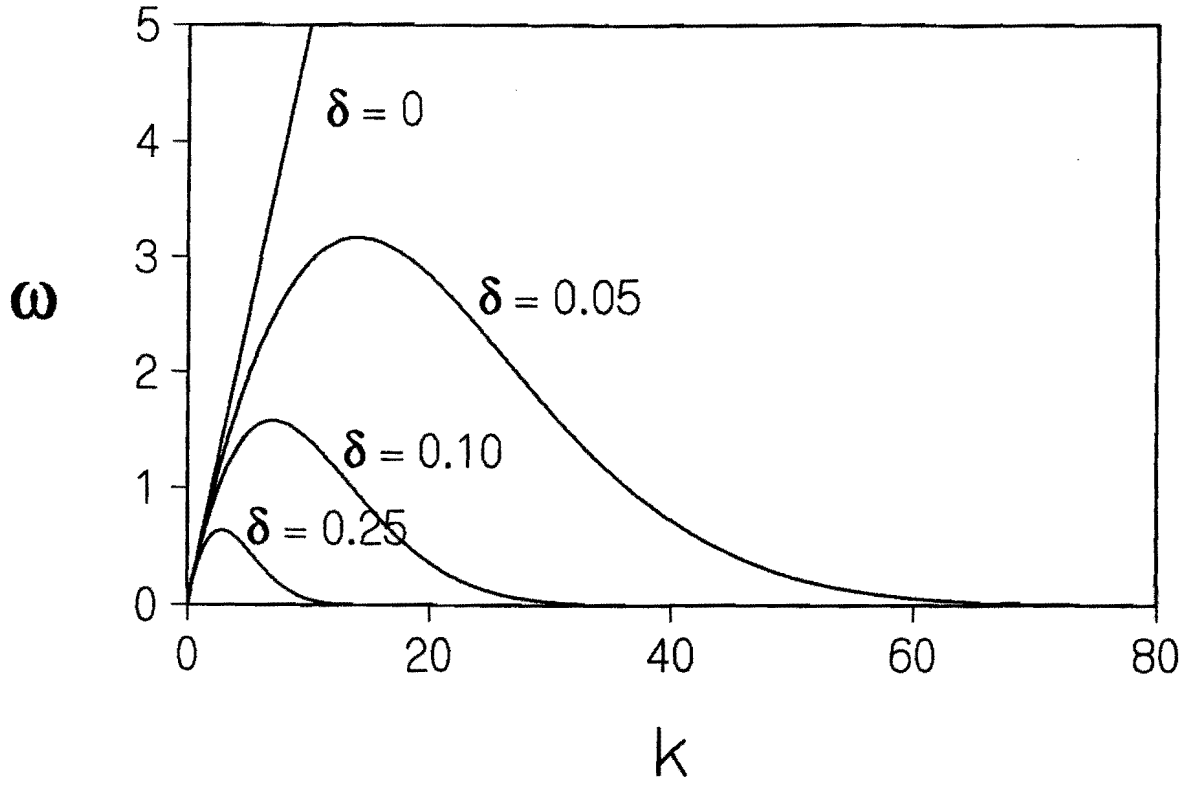

FIG. 3.2. THE LINEAR DISPERSION RELATION $\omega(k)$ USING THE BEALE -MAJDA DESINGULARIZATION FOR DIFFERENT VALUES OF δ. THE STRAIGHT LINE IS THE DISPERSION RELATION OF KELVIN-HELMHOLTZ INSTABILITY ($\delta = 0$).

and for equations (3.11) we have

$$\frac{dx_j}{dt} = \frac{-1}{2N} \sum_{k=1,k\neq j}^{N} \frac{\sinh 2\pi(y_j - y_k) f_{\delta jk}}{\cosh 2\pi(y_j - y_k) - \cos 2\pi(x_j - x_k)} \tag{3.13.a}$$

$$\frac{dy_j}{dt} = \frac{-1}{2N} \sum_{k=1,k\neq j}^{N} \frac{\sin 2\pi(x_j - x_k) f_{\delta jk}}{\cosh 2\pi(y_j - y_k) - \cos 2\pi(x_j - x_k)} \tag{3.13.a}$$

where $f_{\delta jk}$ represent f_δ with x, $\bar{x}$, y, $\bar{y}$ replaced by x_j, x_k, y_j, y_k, respectively. The initial point positions are obtained by

$$x_j = \gamma_j + 0.01 \sin 2\pi\gamma_j \qquad y_j = -0.01 \sin 2\pi\gamma_j. \tag{3.14}$$

Since the two δ's in equations (3.12) and (3.13) have different meanings in the sequel we shall denote the Krasny δ (δ of equations (3.12)) by δ_K and the Beale-Majda δ (δ in equations (3.13)) by δ_{BM}.

Note that the point-vortex approximation is recovered by setting δ_K equal to zero in equations (3.12) and by tending δ_{BM} to zero in equations (3.13).

We have seen that the point vortex approximation method does not converge past the critical time t_c. Now do the previous two approximation methods converge past this time?

We shall try to answer to this question. First consider the case δ_K, δ_{BM} and N fixed. Let the time change for a time step $\Delta t = 0.1$. What happens is shown in figure 3.3 for the case of δ_K and in figures 3.4 for the case of δ_{BM}. In these figures we see that the curves achieve a vertical slope between $t = 1$ and $t = 2$ and rolls up smoothly at later times. For $t > 2$ there is an inner region or core consisting of the turns which become more closely spaced as time progresses. The outer regions become elliptical in shape at later times. For the beale-Majda method we remind that the desingularization has been carried at the end points and their neighboring points, i.e, at $-1, 0, 1$ and 2. In fact the result remains the same as the desingularization is extended to the other points.

For example in fig. 3.4.b. we have extended it to -5 on the left and to 6 on the right. The result, as the figure illustrates does not change.

Next consider the case t and N fixed and let δ_K and δ_{BM} change. The result is shown in figure 3.5 for the case of δ_K and in figure 3.6 for the case of δ_{BM}.

These figures illustrate that the effect of decreasing the desingularization parameter at a fixed time ($t = 1$) greater than the critical time implies a convergence of the sheet. As the desingularization parameters decrease more turns appear in the core.

Last we turn to convergence with respect to N taking δ_K δ_{BM} and t fixed. The result for this is in figures 3.7 and 3.8 for δ_K and δ_{BM} respectively.

This finally shows a convergence as the number of points N is increased. The convergence occurs at any time, even past the critical time ($t_c = 0.375$). The time step was small enough to ensure that for each value of N the point positions are accurate solutions of (3.12), (3.14) and (3.13), (3.14).

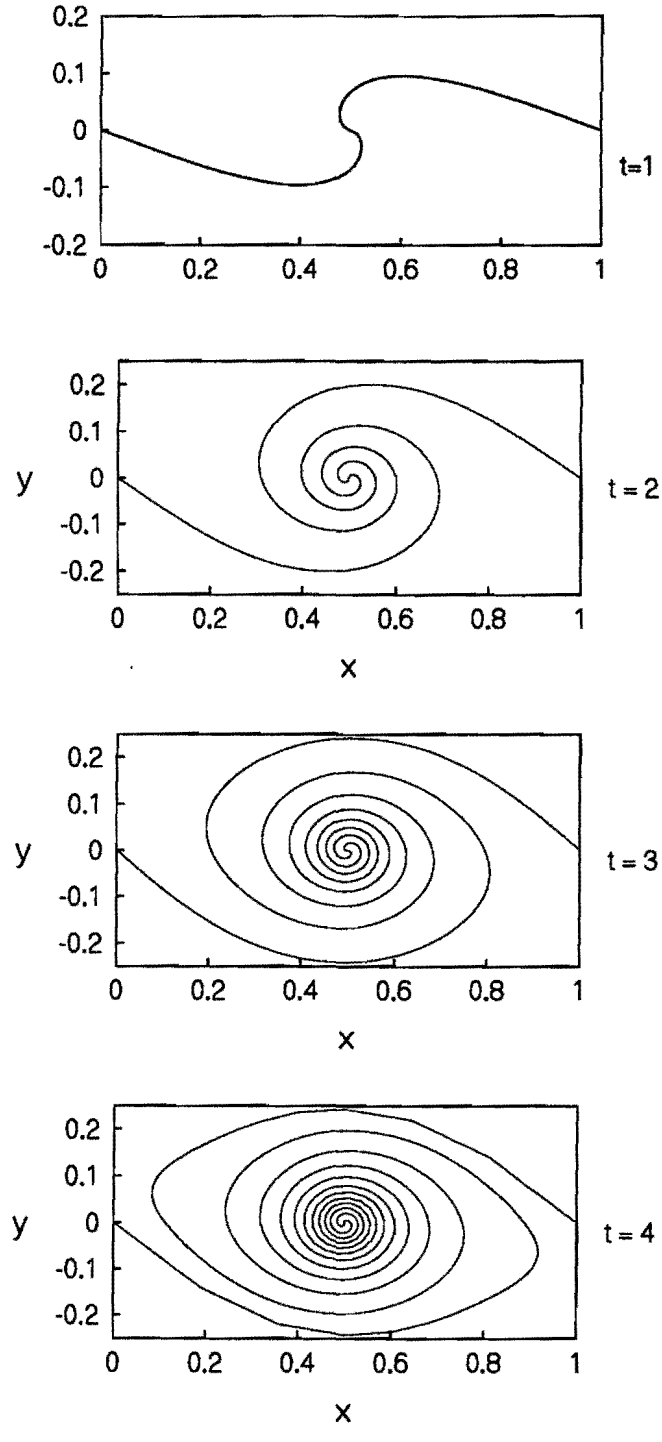

FIG. 3.3. SOLUTION OF THE ORDINARY DIFFERENTIAL EQUATIONS (3.12), (3.14) WITH $\delta_K = 0.25$ AND $N = 400$ AT TIMES $t = 1, 2, 3, 4$.

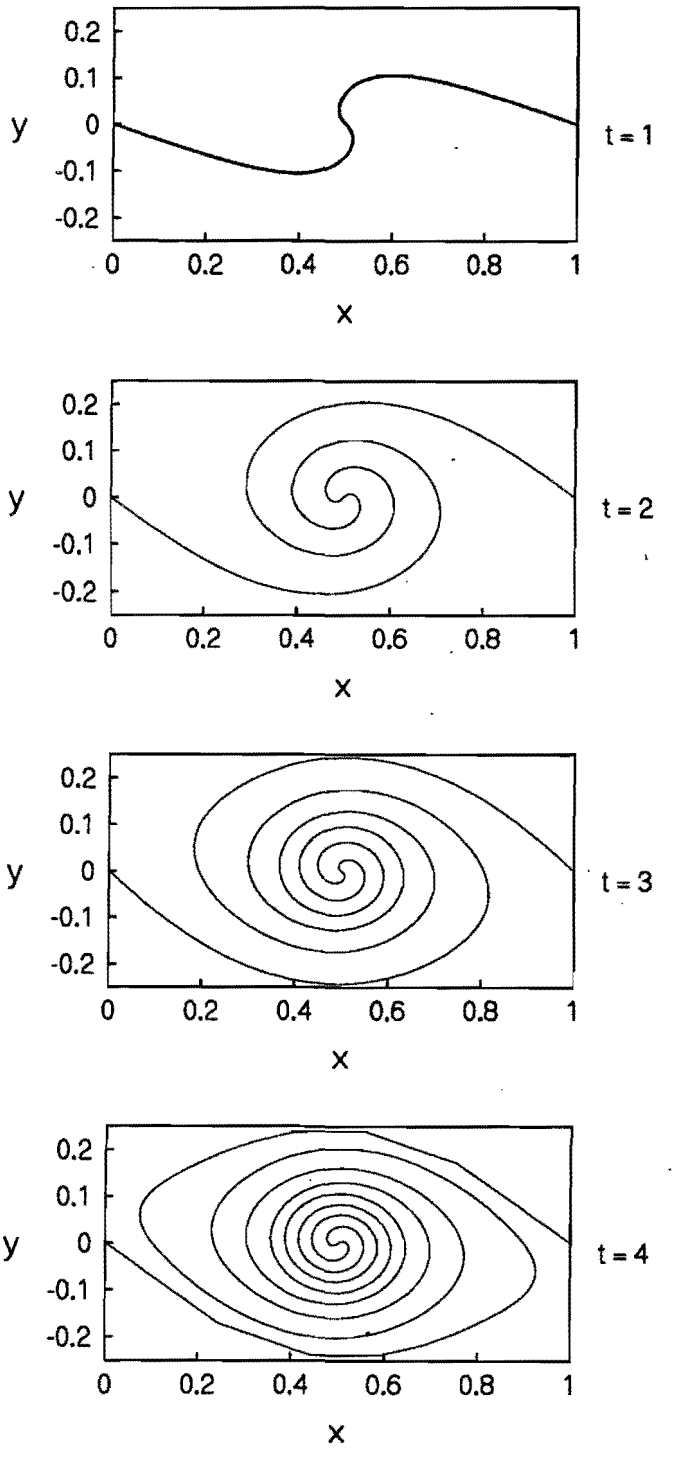

FIG.3.4.A. SOLUTION OF THE ORDINARY DIFFERENTIAL EQUATIONS (3.13), (3.14) WITH $\delta_{BM} = 0.25$ AND $N = 400$ AT TIMES $t = 1, 2, 3, 4$. THE DESINGULARIZATION IS MADE AT $-1, 0, 1, 2$.

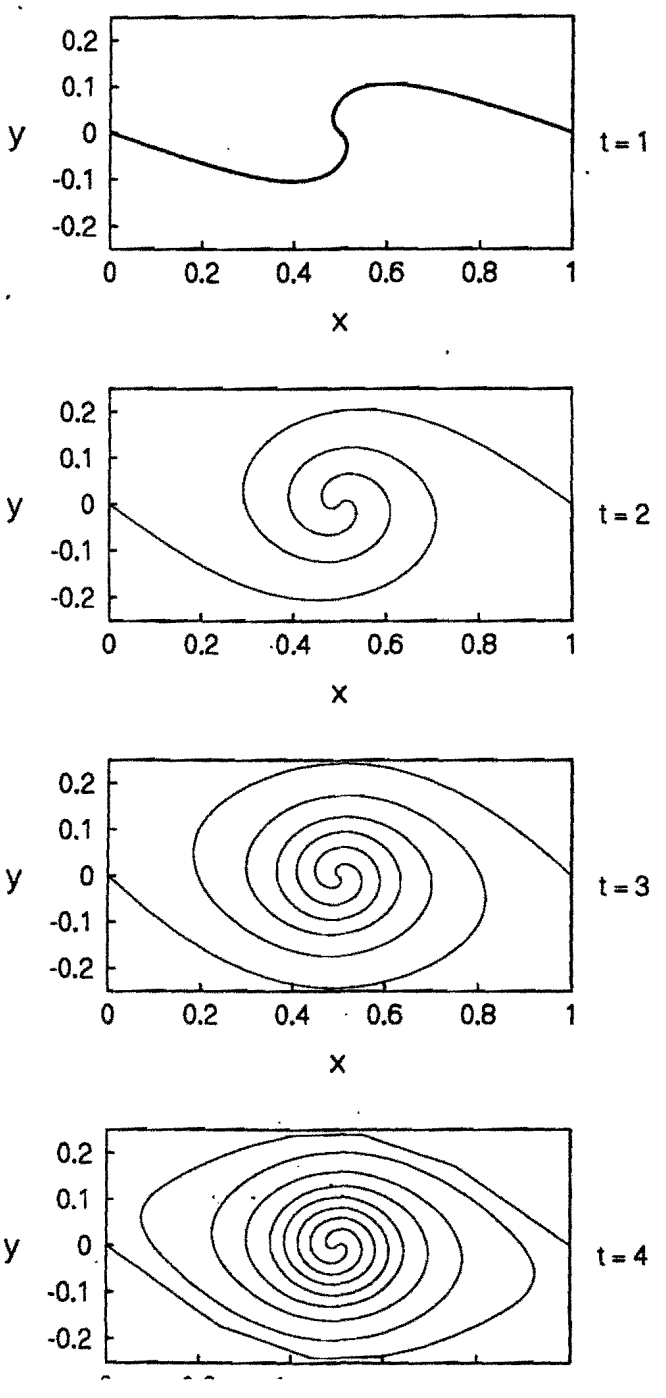

FIG. 3.4.B. SOLUTION OF THE ORDINARY DIFFERENTIAL EQUATIONS (3.13), (3.14) WITH $\delta_{BM} = 0.25$ AND $N = 400$ AT TIMES $t = 1, 2, 3, 4$. THE DESINGULARIZATION IS MADE AT $-5, -4, -3, -2, -1, 0, 1, 2, 3, 4$.

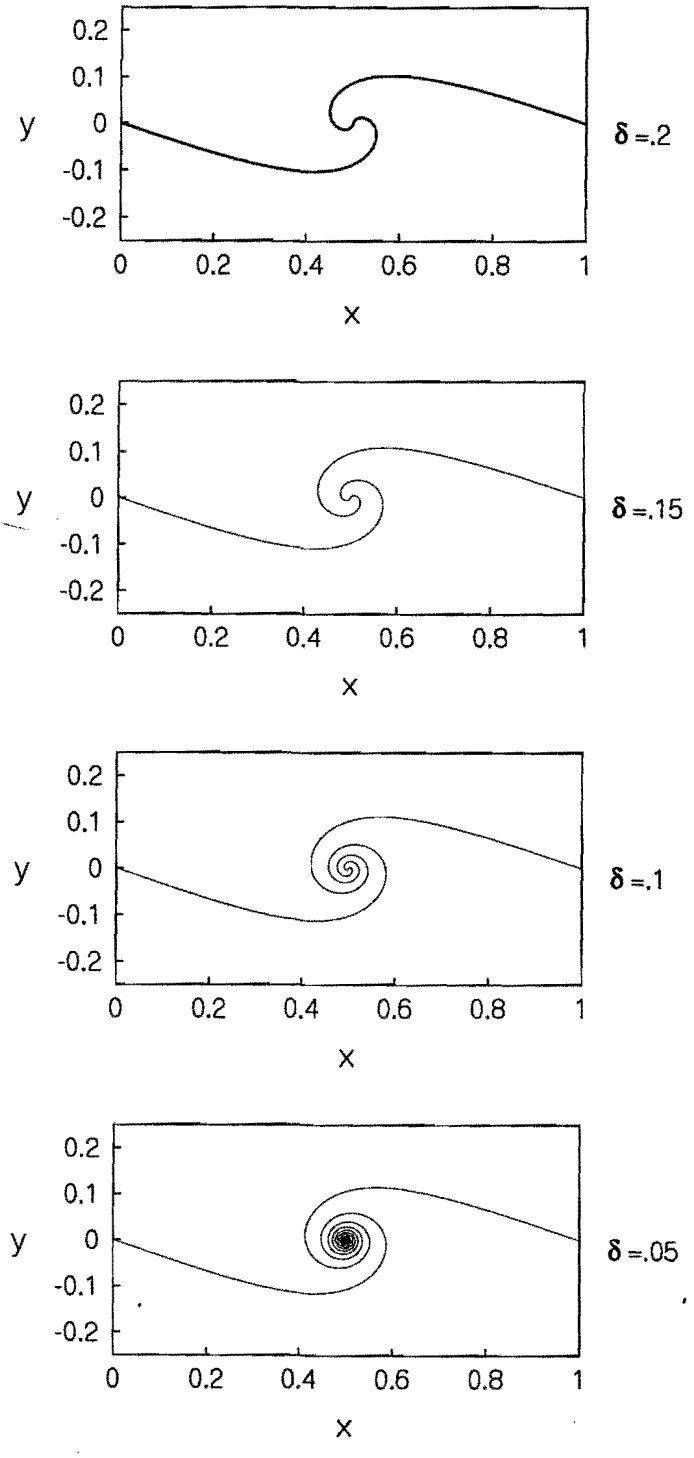

FIG. 3.5. SOLUTION OF THE ORDINARY DIFFERENTIAL EQUATIONS (3.12), (3.13) AT $t = 1$ USING $\delta_K = 0.2, 0.15, 0.1, 0.05$. N=400.

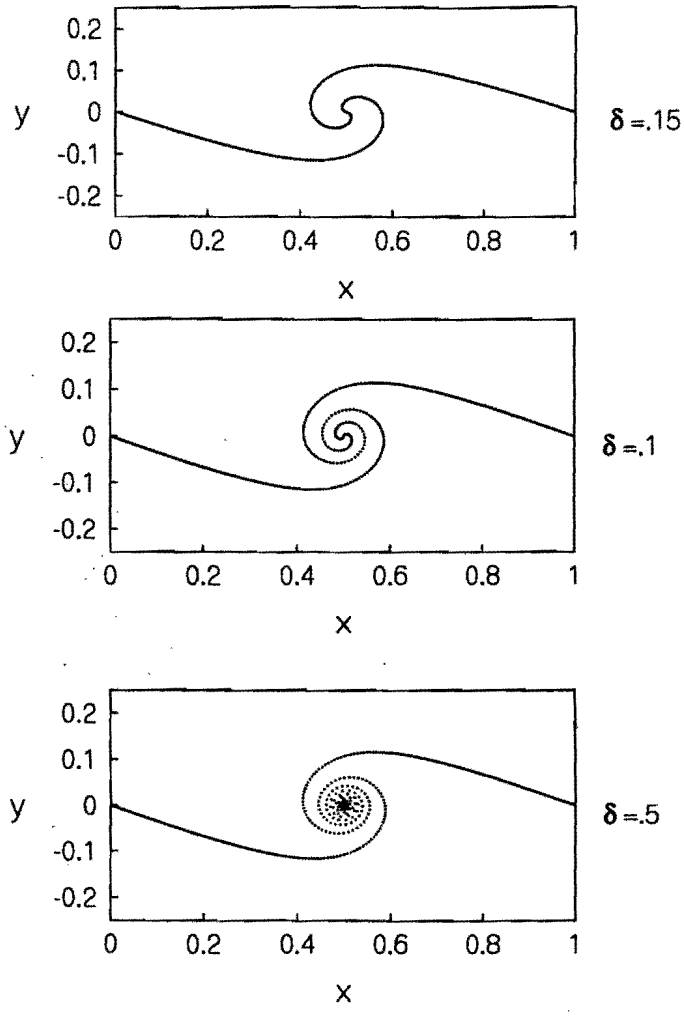

FIG. 3.6. SOLUTION OF THE ORDINARY DIFFERENTIAL EQUATIONS (3.13), (3.14) AT $t = 1$ USING $\delta_{BM} = 0.15, 0.1, 0.05$. N=400.

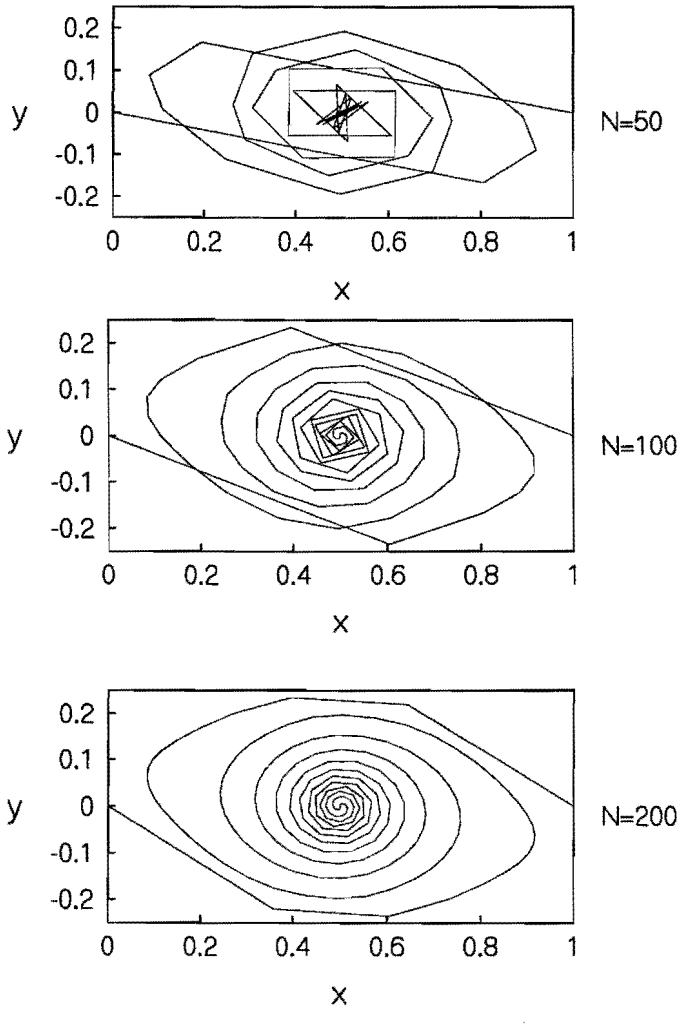

FIG. 3.7. SOLUTION OF THE ORDINARY DIFFERENTIAL EQUATIONS (3.12), (3.13) WITH AT $t = 4$ AND $\delta_K = 0.25$ USING $N = 50, 100, 200$.

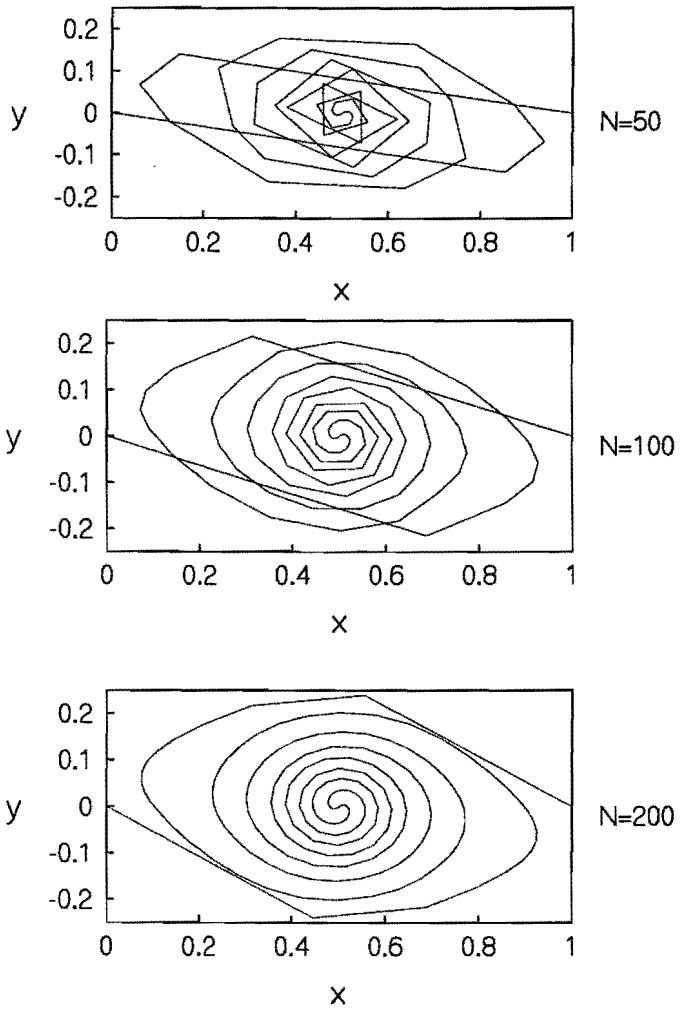

FIG. 3.8. SOLUTION OF THE ORDINARY DIFFERENTIAL EQUATIONS (3.13), (3.13) WITH AT $t = 4$ AND $\delta_{BM} = 0.25$ USING $N = 50, 100, 200$.

4. THE IMPULSIVELY STARTING FLOW

In this chapter we shall discuss a numerical model to represent the impulsively starting flow field in a domain bounded on one side by a wall and on the other side by a circular boundary as shown in fig 4.1. In this figure there is an inflow through a slit. At the entrance of the slit a polynomial fit to the time-dependence of the measured velocity is used as the input and at the semicircle a radial outflow is assumed.

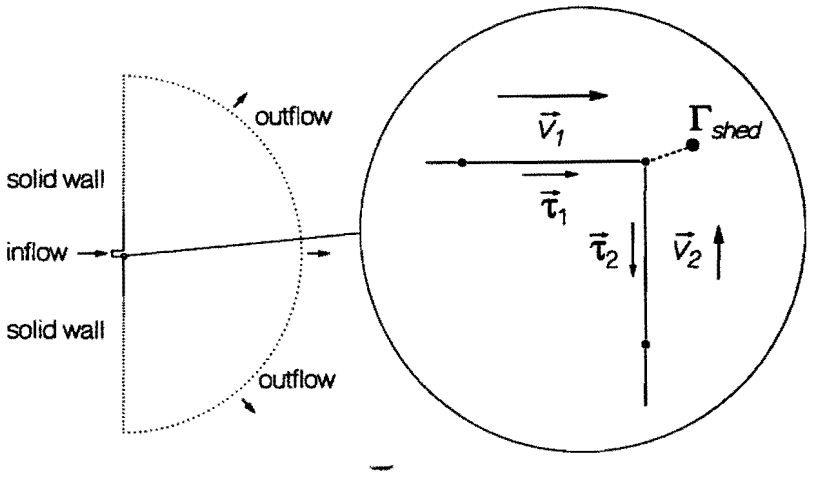

FIG. 4.1. THE COMPUTATIONAL DOMAIN

In reality, what happens in the flow domain, is that, due to the action of viscous forces, vorticity is generated at solid boundaries. In a high Reynolds number flow that starts as a uniform flow, we begin by a region with rotational flow limited to a thin boundary layer near the wall. However at the edge of the slit the rotational boundary layer separates from the wall , thereby forming a free shear layer.

On the other hand, in our computational model we have assumed a potential flow (i.e, inviscid and irrotational) where the separation, by definition, does not occur. Therefore, we need to implement conditions that can bring the model closer to the reality. This will allow us to compare our results with experiment. We do this by weakening our restriction of irrotational flow: we will allow the presence of vorticity in lines and surfaces in the flow. The amount of shed vorticity is not known without additional condition. The velocity induced by this vorticity adds to the singular behavior of the potential flow around the edge. According to the Kutta condition we require the amount of shed vorticity to cancel the singularity and thus ensuring uniqueness for the problem.

The analysis in the previous chapter shows that the shear layer so obtained rolls up infinitely and a representation of it by a row of discrete vortices has a chaotic behavior. In

the sequel we shall use both the Krasny and Beale-Majda desingularization blob methods to describe the shear layer. These two methods are known to stabilize the method that uses point vortices by introducing vortex-blobs. For a vortex blob the vorticity is smoothed out in a small region around the center of the discrete vortex.

4.1. THE NUMERICAL MODEL

The numerical model we shall use to describe the flow field is as follows

We use a boundary element method which is an alternative approximate method to satisfy the boundary condition of zero normal velocity. In this method the boundary is divided into elements (panels) carrying a vortex distribution $\gamma(s)$ and a source distribution $q(s)$.

The tangential and normal velocities jump by an amount of $\gamma(s)$ and $q(s)$ respectively. If we define on each panel j a tangential and normal velocity $(u_j, v_j) = (u(s_j), v(s_j))$ and denote the velocities on the outside of the geometry by (u_j^-, v_j^-) and the velocities on the inside by (u_j^+, v_j^+) then

$$q_j = v_j^+ - v_j^- \tag{4.1.a}$$

and

$$\gamma_j = u_j^- - u_j^+. \tag{4.1.b}$$

4.1.1 Generation of vorticity

The vorticity generation method is accomplished by the introduction of a new vortex at a point which is equal or close to the edge. The initial position of the nascent vortex is determined by the local flow near the edge as

$$\vec{x} = \vec{v}_{\text{shed}} \Delta t$$

$$\vec{v}_{\text{shed}} = \frac{1}{2}(\vec{v}_1 + \vec{v}_2)$$

$$\Gamma_{\text{shed}} = (\vec{v}_1 \cdot \vec{\tau} + \vec{v}_2 \cdot \vec{\tau}) |\vec{v}_{\text{shed}}| \Delta t$$

respectively. Here $\vec{v}_1$, $\vec{v}_2$ are the velocities at the midpoints of the panels that we shall calculate in section 4.1.3. and $\vec{\tau}$ is the tangential unit vector of a panel.

4.1.2 Velocity at a point in the geometry

If the boundary is described by $z(s)$ the velocity at a point z_0 in the computational domain can be obtained from the contribution of the vortex and source distributions on the boundary and the contributions of the singularities (embedded in the inviscid model) inside the flow field.

This yields

$$\frac{\partial z^*}{\partial t} = u - iv = \int \frac{q(s) - i\gamma(s)}{2\pi} \frac{1}{z_0 - z(s)} ds + G_j$$

where s is the arc length along the boundary and G_j is the contribution of the singularities. Using a Krasny desingularization we get

$$G_j = \sum_{j=1}^{NV} K_{\delta_K}(z_0 - z_j)\Gamma_j$$

where Γ_j is the total circulation, NV is the number of vortices and K_{δ_K} is given by

$$K_{\delta_K}(z_0 - z_j) = \frac{1}{2\pi(z_0 - z_j)} \frac{|z_0 - z_j|^2}{|z_0 - z_j|^2 + \delta_K^2}$$

for one point vortex. The vorticity distribution associated with this kernel is given by

$$\omega_j(z) = \frac{\Gamma_j}{2\pi} \cdot \frac{2\delta^2}{(|z - z_j|^2 + \delta^2)^2}.$$

A Beale-Majda desingularization gives

$$G_j = \sum_{j=1}^{NV} K_{\delta_{BM}}(z_0 - z_j)\Gamma_j$$

with $K_{\delta_{BM}}$ given by

$$K_{\delta_{BM}}(z_0 - z_j) = \frac{1}{2\pi(z_0 - z_j)}(1 - e^{-\frac{|z_0 - z_j|^2}{\delta_{BM}^2}})$$

for one point vortex with a Gaussian vorticity distribution

$$\omega_j(z) = \frac{\Gamma_j}{2\pi} \cdot \frac{2}{\delta^2} e^{\frac{-|z - z_j|^2}{\delta^2}}.$$

4.1.3. velocity at the midpoint of a panel

To obtain the velocity at the midpoint of the panel $z(s_j^m)$ we need the contributions of the vortex and source distributions, the contributions of the other panels and the contributions of the singularity points.

Since at the j-th panel equations 4.1 are satisfied and since a panel does neither introduce a normal velocity to itself, i.e,

$$0 = v_j^+ - v_j^-$$

nor a tangential velocity to itself, i.e,

$$0 = u_j^- - u_j^+$$

we have at the j-th panel

$$(u + iv)_j^{\pm} = \mp\frac{1}{2}(\gamma_j - iq_j)$$

where $\gamma_j = \gamma(s_j)$ and $q_j = q(s_j)$.

Thus the velocity in the midpoint is given by

$$(4.2) \qquad (u - iv)^{\pm}(z(s_j^m)) = \mp\frac{1}{2}(\gamma_j - iq_j) + \int \frac{q(s) - i\gamma(s)}{2\pi} \frac{1}{z_0 - z(s)}\, ds + G_j$$

where the principle value is taken in the integral.

4.1.4. Determination of vortex distribution on each panel

As a result the only unknown in the expression of the velocity is the vortex distribution. The source distribution is determined by the inflow velocity. The vortex distribution is obtained by imposing the integral equations (4.2) at a number of collocation points. For this first order scheme, with panel-wise constant vortex and source distribution γ_j and q_j, respectively the collocation points are chosen as the midpoints of the panels.

By imposing a Dirichlet boundary condition, that is, by implementing a zero tangential velocity on the outside of each panel j, $j = 1, \cdots, np$, where np is the number of panels, from (4.2) we get the following discretized integral equations.

$$0 = \frac{1}{2}\gamma_j + \sum_{k=1, k\neq j}^{np} \gamma_k K_\gamma(j,k) + \sum_{k=1, k\neq j}^{np} q_k K_q(j,k) + \sum_{k=1, k\neq j}^{nv} \Gamma_k K_\Gamma(j,k)$$

for $j = 1, \cdots .np$ where $K(j,k)$ are the aerodynamic influence coefficients (a.i.c.) which determine the influence of the vortex distribution on panel k exercised at the midpoint of panel j. The a.i.c. K_γ and K_q only depend on the geometry. The a.i.c. K_Γ determines the induced velocity by discrete vortices of unit circulation at point $z = z_k$ at the midpoint of panel j. Since the discrete vortices convect with the flow, the a.i.c. K_Γ is time-dependent and has to be calculated each time step.

The a.i.c.'s are calculated by

$$K_\gamma(j,k) = \Re\Big(\frac{-1}{2\pi i \frac{dz}{ds}|_{s_k^m}} \frac{dz}{ds}|_{s_j^m} \ln\Big(\frac{z_j^m - z_{k+1}}{z_j^m - z_k}\Big)\Big),$$

$$K_q(j,k) = \Re\left(\frac{-1}{2\pi \frac{dz}{ds}|_{s_k^m}} \frac{dz}{ds}|_{s_j^m} \ln\left(\frac{z_j^m - z_{k+1}}{z_j^m - z_k}\right)\right),$$

$$K_\Gamma(j,k) = \Re\left(\frac{-1}{2\pi i \frac{dz}{ds}|_{s_k^m}} \frac{dz}{ds}|_{s_j^m} \ln\left(\frac{1}{z_j^m - z_k}\right)\right).$$

In these equations s denotes the coordinate along a panel, z_k and z_{k+1} the two edgepoints of panel k. In matrix for equations (4.3) can be written as

$$[K_\gamma]\{\gamma\} = -[K_q]\{q\} - [K_\Gamma]\{\Gamma\} \tag{4.4}$$

where the right-hand side is known for every time step.

4.2. Numerical results

The numerical scheme

1. For a given inflow velocity and known positions of all the discrete vortices the vortex distribution is calculated by equation (4.4). The velocity at a point in the geometry is then calculated by the formula of the velocity in section 4.1.2.
2. A step forward in time is taken using a fourth order Runge-Kutta integration scheme. All the vortex blobs are convected with the flow and a marker is released at the edgepoint of the slit. The marker represent the nascent vortex defined in section 4.1.1. and it moves with the local flow velocity.
3. Finally a new vortex is generated with a circulation as in section 4.1.3. Now the loop starts again from 1.

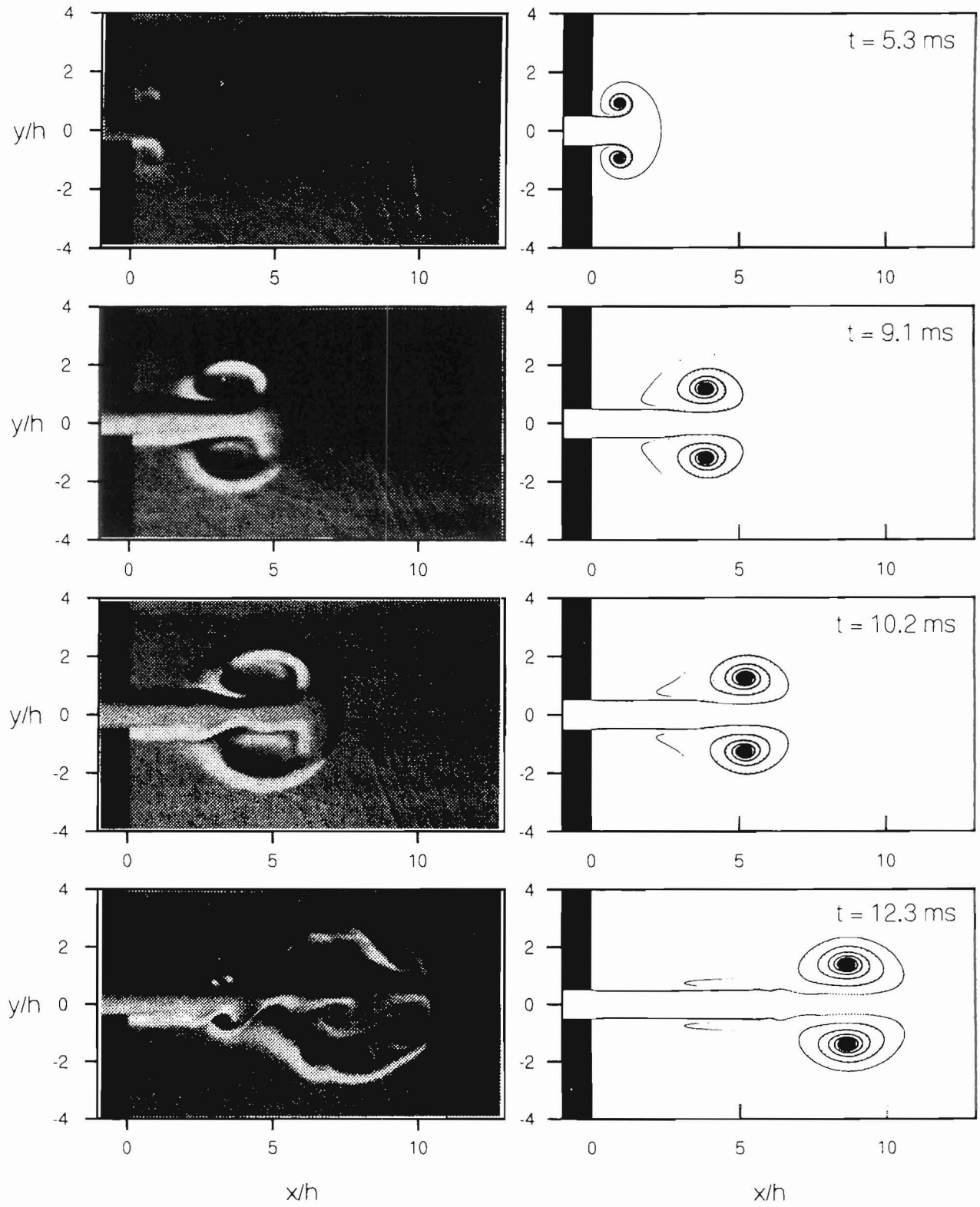

FIG. 4.2 FLOW VISUALIZATION AND NUMERICAL SIMULATION USING THE KRASNY DESINGULARIZATION WITH $\delta = \sqrt{\nu \cdot t}$

Results

The results of the numerical scheme using the Krasny desingularization and the experimental results using flow visualization[1] are shown in fig. 4.2. The desingularization parameter is chosen to be time-dependent in order to simulate a growing shear layer.

Like the shear layer growth of a one-dimensional infinite shear layer the time-dependence was taken as $\delta_K = \sqrt{\nu t}$, where ν is the kinematic viscosity of air. The time-step of the simulation is $13.4\,10^{-6}s$.

In the experiment we see the formation of a jet and a vortex pair that proceeds it. After $10ms$ instabilities appear in the jet structure in the form of smaller vortices. After $12ms$ the whole structure has been broken up into a set of smaller vortices and after $14ms$ the flow has become chaotic. The simulation shows similar results except that instabilities appear only after $12ms$. This opens the question whether the instabilities are of numerical or physical nature. For this reason we tried to see what happens if we change the desingularization method from Krasny method to Beale-Majda method. The results of the simulation are shown in fig. 4.3. For this calculation we have taken $\delta_{BM} = \sqrt{2\nu t}$. Again the same features appear but now they are more pronounced than in the Krasny method. This may be due to the "long-tail" of the vorticity distribution in the Krasny method while in the case of the Beale-majda method the vorticity drops off exponentially with the square of the distance to the center of the blobs.

For more details concerning comparison of these methods as well as experimental issues we refer to the forthcoming paper [HVDH].

In conclusion we can say that both (Krasny and Beale-Majda) simulations agree very well until the time when instabilities appear. The experiment shows the instabilities earlier than the simulations. This may certainly be due to the smoothed velocity that was used as input for the simulations. The question whether the instabilities are physical or numerical is still open.

[1] For details concerning flow visualization see the appendix at the end

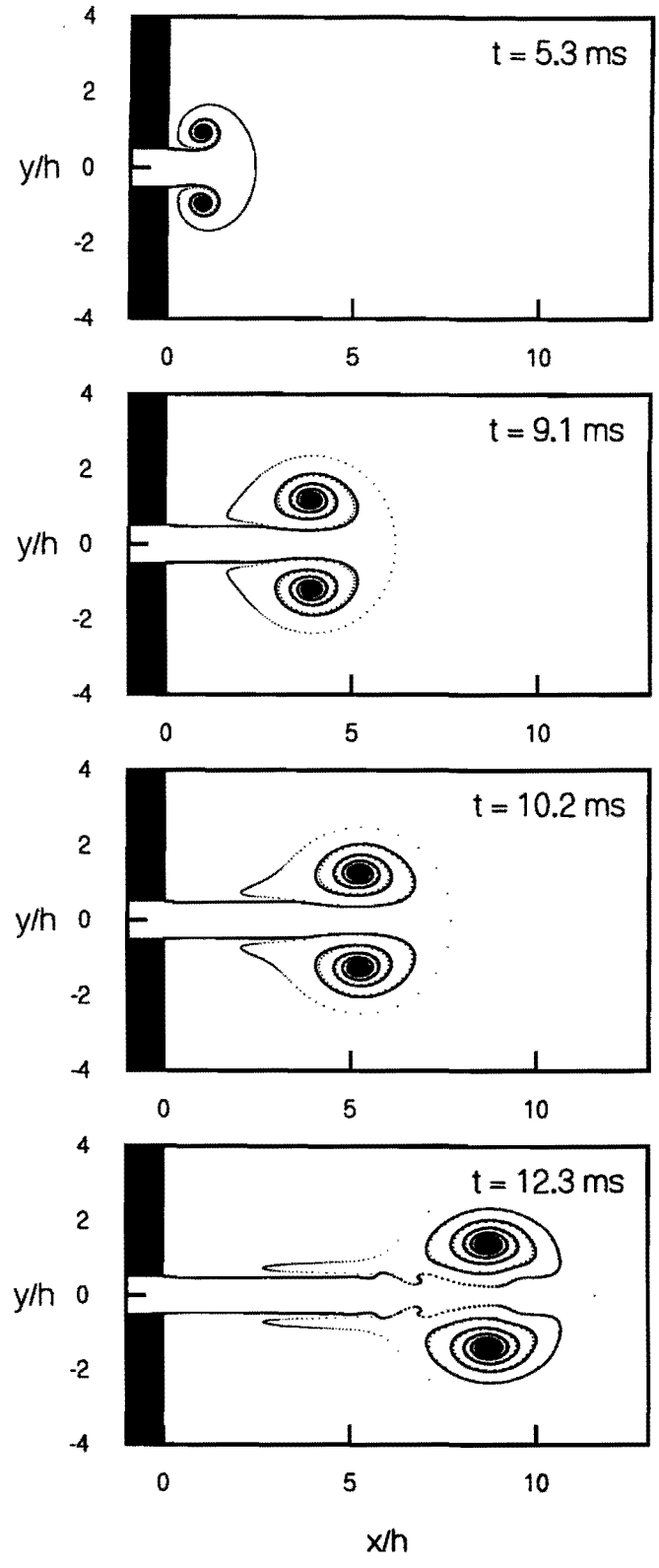

FIG. 4.3. FLOW VISUALIZATION AND NUMERICAL SIMULATION USING THE BEALE-MAJDA DESINGULARIZATION WITH $\delta = \sqrt{2\nu \cdot t}$

APPENDIX: UNSTEADY FLOW THROUGH 2-D IN VITRO MODELS OF THE HUMAN GLOTTIS[2]

1 INTRODUCTION

For the development of a physical model of voiced sound production it is important to capture both the mechanical behaviour of the vocal folds as well as the fluid dynamical aspects of the air flow through the glottis, because the flow determines the hydrodynamical force on the vocal folds and the movement of the vocal folds determines the flow. Concerning the first point we refer to the papers by Titze (1975) and Scherer (1991) who discuss the mechanical properties of the vocal folds. It is the second point where our interest lies: a description of the unsteady flow through the glottis. The actual modelling of voiced sound production is done in cooperation with the Institute for Perception Research (IPO, Eindhoven, Netherlands) and the Institut pour la Communication Parlée (INPG, Grenoble, France).

To fully concentrate on the fluid dynamical aspects a rigid (scale) model of the human glottis is realized. Instead of applying a steady pressure over moving vocal folds, an unsteady pressure is applied over rigid stationary vocal folds. Care is taken that the relevant parameters describing the flow through the glottis have the correct values. In the glottis these parameters are the Strouhal number (typically of order 10^{-2}) and the Reynolds number (typically of order 10^4). The Strouhal number is a measure for the influence of the unsteadiness on the flow and the Reynolds number reflects the importance of viscous effects on the flow. Based on the values of these parameters we suspect that a quasi-steady frictionless bulk flow model suffices to describe most of the fluid dynamics. The effect of viscosity is described within the boundary layer approximation. However, accurate prediction during the closing of the vocal folds requires an essentially unsteady model. Such a model taking into account these effects has been proposed by Pelorson (1994) The aim of our study is to determine the limits of validity of the simple model of Pelorson.

In this paper we will present pressure and velocity measurements in two different models of the glottis: a right-angled (reference) model and a round (liplike) model. Furthermore we will show some flow visualizations and compare the details of the unsteady jet formation with a potential flow model based on a desingularized point vortex method.

2 EXPERIMENTAL SETUP

In figure 1 schematic drawings of the two setups are shown. The two setups are basically the same except that the right-angled constriction in figure

[2]This has been reproduced (with agreement of the authors) from the work of G. Hofmans, J. den Doelder, E.A.I van de Ven, A. Hirschberg and A.P.J. Wijnands in the Technical University of Eindhoven

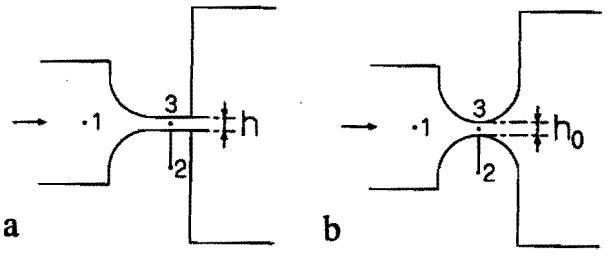

Figure 1: Glottis geometries; (a) right-angled, (b) round

1a is replaced by the round constriction in figure 1b. The arrow indicates the direction of the flow. The whole setup is situated in a room in which a pressure lower than the surrounding laboratory can be created. The pipe upstream of the constriction connects the setup with the laboratory so that when the room pressure is less than the atmospheric pressure in the laboratory a flow through the setup is realized. The flow can be stopped by a mechanical valve between the laboratory and the pipe. Although this pipe is round with a diameter of 30 mm and the rest of the setup is rectangular with a width of 30 mm it does not seem to influence the two-dimensionality of the flow though the constriction in a significant way. The channel downstream of the constriction has a height of 74 mm and has a lenght of 64 mm. Therefore the setup does not strictly represent the flow through a channel with a constriction. Since we are interested in the flow through the glottis for a known pressure difference Δp over the glottis and we want to check some simple models describing this flow, the exact height of this part of the setup is not so important. The height and lenght of this part, however, assure that the pressure downstream of the constriction is zero; the pressure in the room is our reference pressure therefore this pressure is defined as being zero.

The right-angled constriction consist of a pair of quarter-cylinder blocks (radius of cuvature is 10 mm) followed by a straight narrow channel (lenght 10 mm) that has a height h of 3.25 mm. The round geometry consist of two half-cylinders (radius of curvature R is 10 mm) which form a converging-diverging channel with a minimum aperture h_0 of 3.42 mm. The whole setup approximately represent a 3:1 scale model of the human glottis.

An unsteady pressure difference over the glottis is obtained by a fast opening of the valve. The valve is a metal slide that can be shot away using a spring. The opening time of the valve is approximately 20 ms. The pressure change is measured at position 1 and position 2 (see figure 1) using two calibrated piezoelectric transducers (PCB type 116A) in combination with charge amplifiers (Kistler type 5011). The transducer at position 1 is placed in the side wall of the channel. The other transducer at position 2 is situated inside the lower cylinder block and measures the pressure change via a narrow opening of 0.3 mm along the whole width of the channel. At position 3 (see figure 1) the velocity is measured by means of hot-wire anemometry. The pressure range of this setup is from 50 Pa to 700 Pa, which implies a velocity range from 9 m/s to 34 m/s.

Flow visualizations are obtained with a Schlieren technique. The refractive index contrast is provided by injecting a mixture of 50% argon and 50% neon just upstream of the constriction. This mixture is bouyancy neutral so that gravity will not effect the flow of this mixture.

3 RESULTS

In figure 2 a typical pressure measurement is presented for the right-angled glottis model. As one can observe, the pressure changes from zero to 467 Pa in about 30 ms. If we define the Strouhal number $Sr = f_0 \cdot l/u_0$ and the Reynolds number $Re = h \cdot u_0/\nu$ in which f_0 is a typical frequency, l a typical lenght scale (length of channel), u_0 a typical velocity, h a typical height, and ν the kinematic viscosity of air ($\nu = 1.5 \cdot 10^{-5}$) and we insert $f_0 = 1/(4 \cdot 0.03) \approx 8$ Hz, $l = 10$ mm , $u_0 = 27$ m/s, $h = 3$ mm we find $Sr \approx 0.01$ and $Re \approx 5000$ which agrees well with the values in the glottis.

The pressure p_2 measured at position 2 also slightly differs from zero although this was not expected based on the Reynolds number. However, carefull steady pressure measurements have shown that a steady pressure of about 4% of the steady pressure p_1 can be expected. These measurements agree very well with a simple boundary layer model as proposed by van Zon (1990). The fast oscillations in the pressure signals just before the rise are due to mechanical vibrations originating from the valve opening transmitted by the pipe. Also at the beginning of the pressure rise a small hump can be observed. The origin of this still remains obscure.

The main flow can be described by an incompressible inviscid model. So the velocity at position 3 can be calculated from the pressure differ-

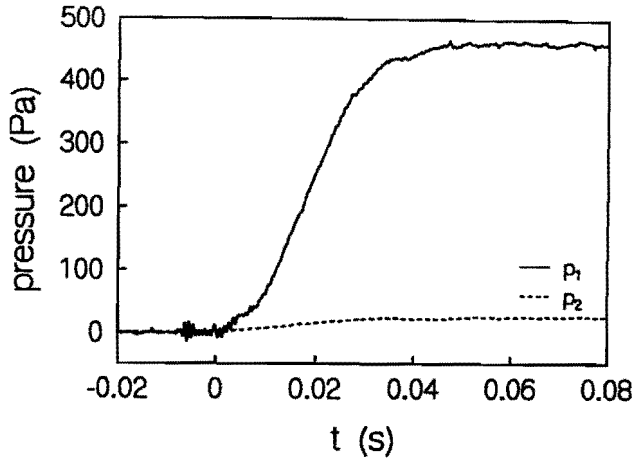

Figure 2: A typical pressure measurement. p_1 is measured at position 1 and p_2 is measured at position 2 for the right-angled glottis model.

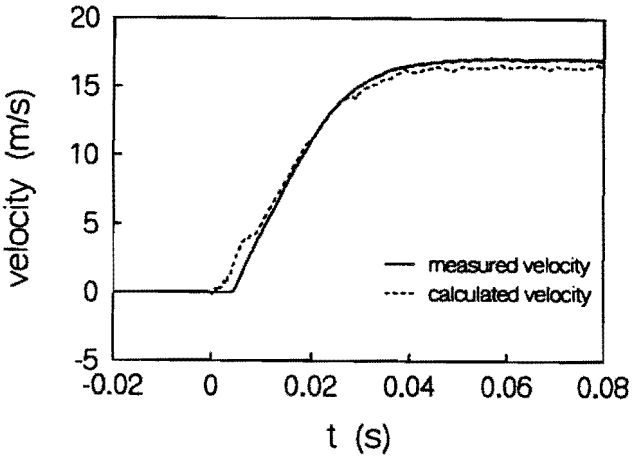

Figure 3: Measured velocity and calculated velocity after integration of equation (3) for the right-angled glottis model. Steady $\Delta p = 178$ Pa.

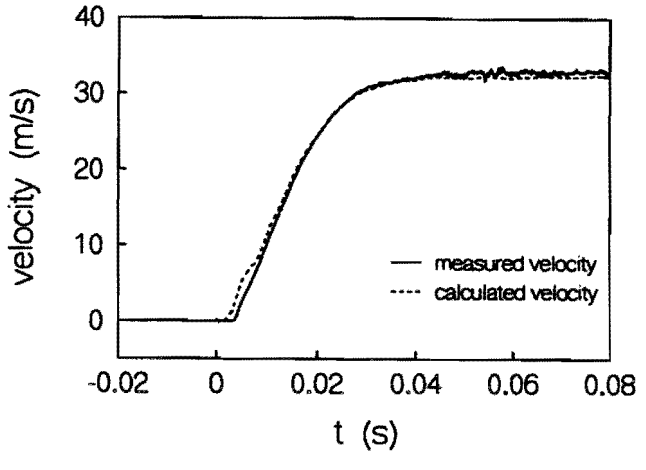

Figure 4: Measured velocity and calculated velocity after integration of equation (3) for the right-angled glottis model. $\Delta p = 677$ Pa.

ence $p_1 - p_2$ using the unsteady Bernoulli equation

$$\rho\frac{\partial\varphi_1}{\partial t} + \frac{1}{2}\rho u_1^2 + p_1 = \rho\frac{\partial\varphi_2}{\partial t} + \frac{1}{2}\rho u_2^2 + p_2 \qquad (1)$$

where ρ is the density of air, φ the velocity potential, u the velocity and the subscripts refer to the position. Assuming a uniform velocity profile the potential difference $\varphi_2 - \varphi_2$ can be expressed as an effective length L_{eff} times the velocity u_2:

$$\varphi_2 - \varphi_1 = \int_1^2 u\mathrm{d}x = u_2 \int_1^2 \frac{h_2}{h(x)}\mathrm{d}x = u_2 \cdot L_{eff} \qquad (2)$$

where we have made use of the conservation of the volume flux $Q = u(x) \cdot h(x) \times width = \text{constant}$. Together these relations lead to the following differential equation for the velocity in position 2:

$$L_{eff} \cdot \rho\frac{\partial u_2}{\partial t} + \frac{1}{2}\rho u_2 \left(1 - \left(\frac{h_2}{h_1}\right)^2\right) = p_1 - p_2 \qquad (3)$$

The overall agreement between the velocity calculation and the velocity measurement is very good for high steady pressures ($\Delta p > 350$ Pa), except for the initial phase of the opening of the valve, and reasonably good for low steady pressures (see figures 3 and 4). The difference between measurement and calculation is less than 1% for high steady pressures and less than 3% for low steady pressures and therefore within the experimental accuracy after the initial phase. The discrepancy at the initial phase is apparently related to the hump that is observed in the pressure signal p_1. As stated before we still have to find an explanation for this.

In figure 5 a typical pressure measurement for the round glottis model is shown. What is striking of this figure is that for the round model we see the hump not only appear in p_1 but also in p_2 and that the pressure p_2 initially rises. This rise can be explained by the fact that the initial flow is much like a potential flow which means that the pressure rise in the throat is one half times the total pressure drop. After this initial stage flow separation occurs (a jet is formed) and the pressure at the throat becomes less than zero: at the throat the velocity has the highest value which implies the lowest pressure. The boundary layers separated in the diverging part of the glottis. The pressure downstream of the glottis is zero which means that the pressure at the throat is less than zero.

Like for the right-angled glottis model equation (3) can be integrated. The result for two different

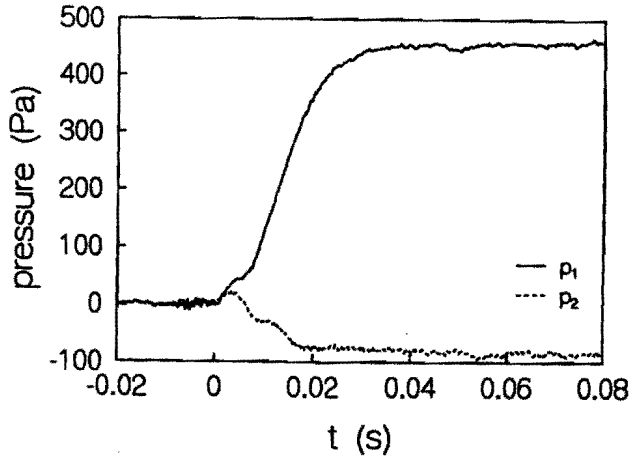

Figure 5: A typical pressure measurement. p_1 is measured at position 1 and p_2 is measured at position 2 for the round glottis model.

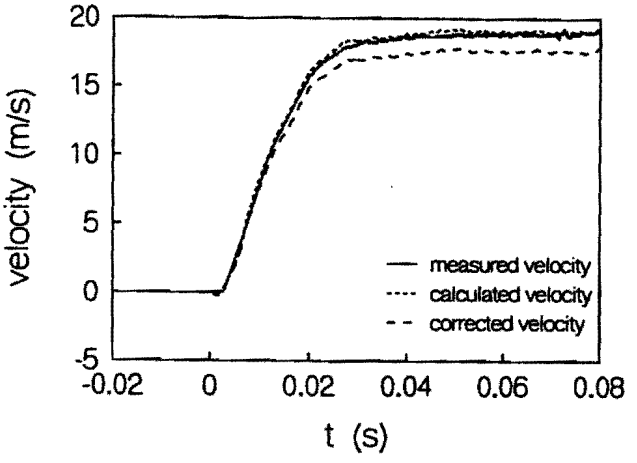

Figure 6: Measured velocity and calculated velocity after integration of equation (3) for the round glottis model. Also the correction is shown. $\Delta p = 184$ Pa.

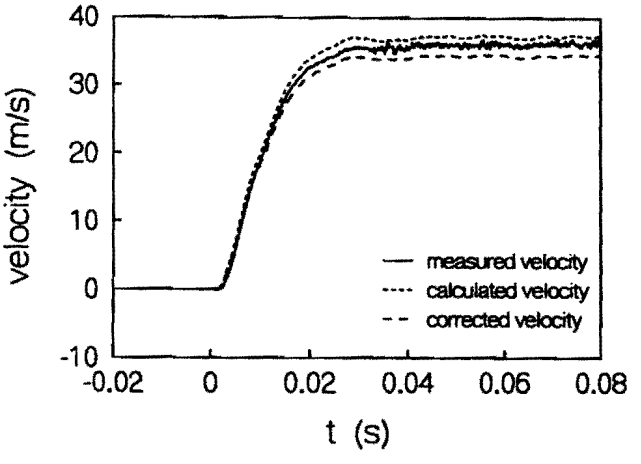

Figure 7: Measured velocity and calculated velocity after integration of equation (3) for the round glottis model. Also the correction is shown. $\Delta p = 680$ Pa.

steady pressures is shown in figures 6 en 7. E cause the pressure is measured at the wall and t velocity is measured in the middle of the thro a small difference between the measured veloci and the calculated velocity is to be expected due a centrifugal contribution to the pressure in radi direction. An analysis of potential flow throu a curved constriction has given the result (radi momentum balance):

$$\frac{\partial p}{\partial r} = \frac{\rho u^2}{R_{eff}} \qquad (4$$

with R_{eff} estimated as two times the radius c curvature R. This leads to a velocity differenc between the calculated velocity and the measure velocity:

$$\Delta u = \frac{h}{4R} \cdot u. \qquad (5$$

In figures 6 and 7 this correction is also shown The overall result for the round glottis model i the same as for the right-angled model with one bi difference that the hump that led to a discrepanc between the calculated velocity and the measure velocity at the initial stage of the valve opening nc longer appears in the velocity signals. Again we see a better agreement for high steady pressures than for low pressures (after correction).

Figures 8 and 10 show the flow visualizations for the right-angled glottis and the round model respectively. Both show symmetric vortex structures that become unstable after a short time. For the round model this symmetry means that on the time scale of the experiment the Coanda effect did not have time to appear. Therefore it is unlikely that for unsteady flow conditions the Coanda effect is important. It is a typical effect that appears in steady flow conditions. To study the details of jet formation numerical simulations have been carried out for the right-angled model. The numerical model is a potential flow with desingularized point vortices. The desingularization used was proposed by Krasny (1987). To take into account the diffusion of vorticity in the shear layer the so-called desingularization parameter δ was made time dependent according to $\delta \propto \sqrt{\nu t}$. As input of the calculation a velocity profile as a function of time measured inside the narrow channel was used. This velocity profile was smoothed for the simulation because the measured profile led to a very unstable calculation. The measured signal not only contained the noise but also the results of the discretization of the hot-wire signal by the

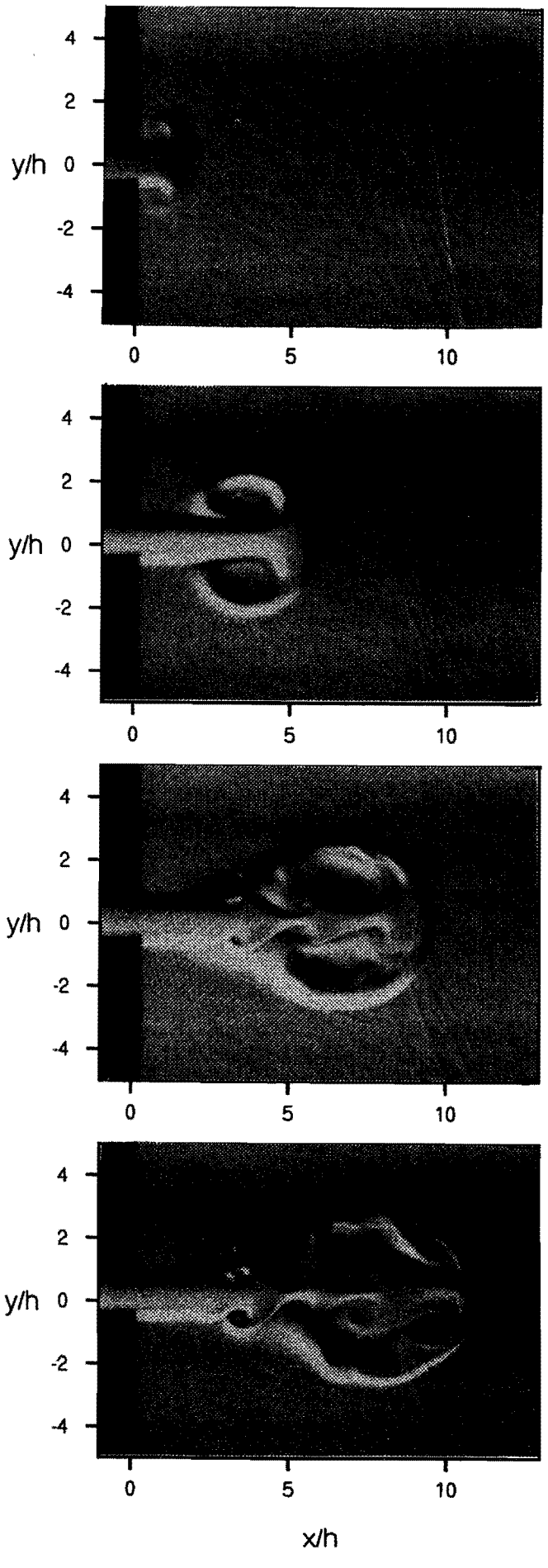

Figure 8: Flow visualization right-angled model: $t_1 = 5.3$ ms, $t_2 = 9.1$ ms, $t_3 = 11.3$ ms, $t_4 = 12.3$ ms top to bottom, $\Delta p = 394$ Pa, $h = 3.40$ mm.

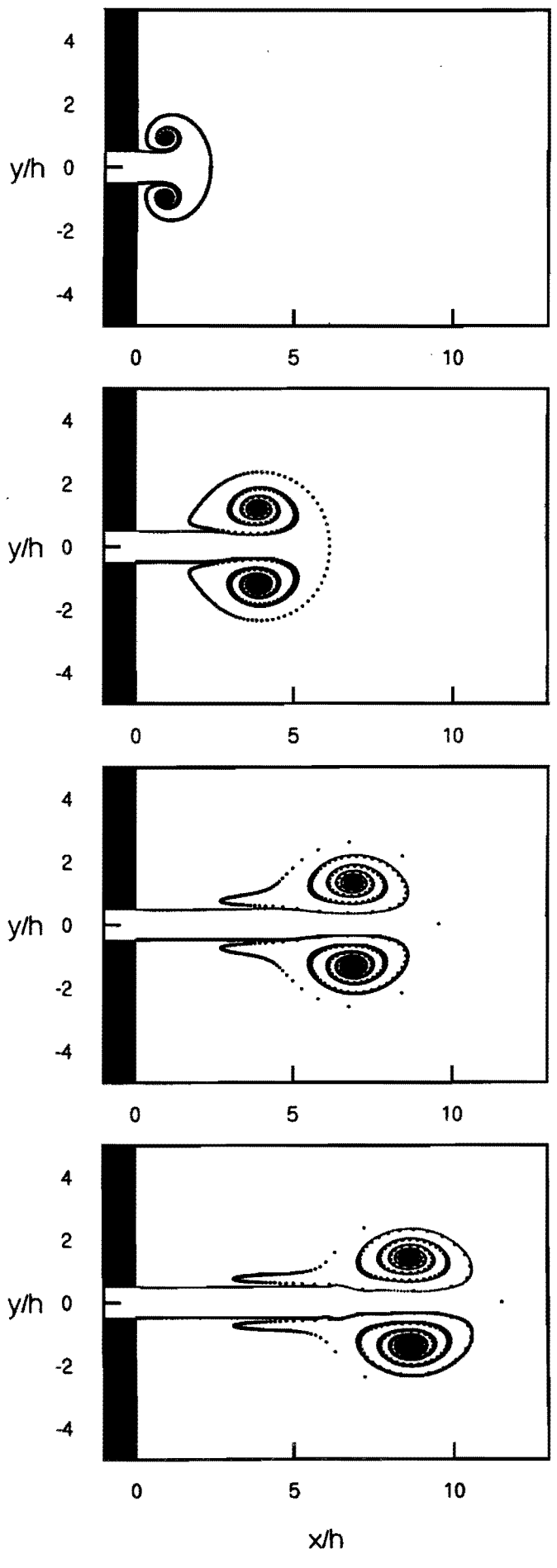

Figure 9: Numerical simulation: $t_1 = 5.3$ ms, $t_2 = 9.1$ ms, $t_3 = 11.3$ ms, $t_4 = 12.3$ ms top to bottom, $\Delta p = 394$ Pa, $h = 3.40$ mm, $\delta = \sqrt{\nu \cdot t}$.

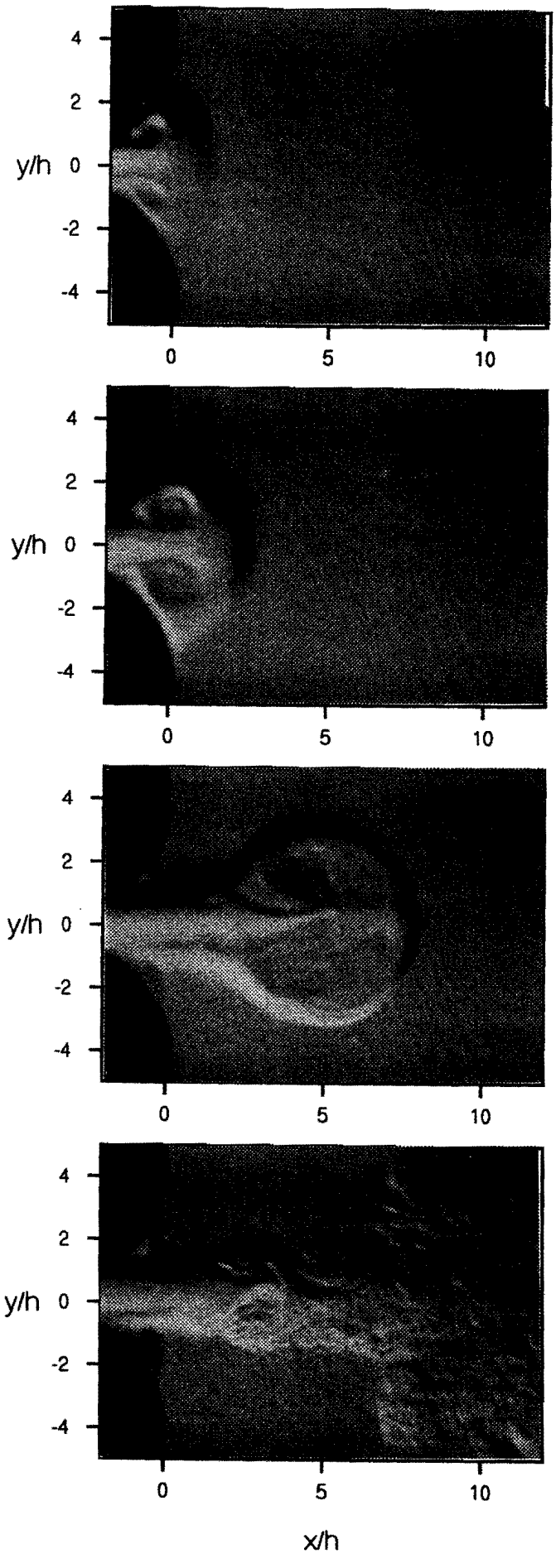

Figure 10: Flow visualization round model: $t_1 = 5.3$ ms, $t_2 = 6.4$ ms, $t_3 = 9.1$ ms, $t_4 = 12.2$ ms top to bottom, $\Delta p = 671$ Pa, $h_0 = 3.42$ mm.

AD-conversion. Figure 9 shows the result of this calculation. The features of the jet formation are captured by the numerical simulation although the visualization show that the experiment is more unstable than the simulation. This could be due to the smoothing of the velocity as a function of time. The smoothing leads to the removal of small velocity variations that can be the trigger of the instability.

4 CONCLUSIONS

The comparison of the measured velocity and the calculated velocity shows that an incompressible inviscid description of the main flow is an accurate representation of reality. The results for steady pressures above 350 Pa agree within 1 % for the right-angled glottis model. However, a larger discrepancy is observed at the initial stage of the valve opening. This is due to a hump in the pressure signal. An explanation for this hump has not yet been found. Such details are not expected to be relevant for the prediction of the oscillations of the vocal folds but for speech models these effect can be quite relevant since details do influence speech quality. For lower pressures the agreement is somewhat less but still within 3%.

For the round glottis model the overall difference is somewhat larger than for the right-angled glottis model, 4% for high pressures and 6% for low pressures, although now the discrepancy at the initial stage due to the presence of the hump in the pressure signals has disappeared. The results show that a correction for the the centrifugal forces is necessary. As the correction is calculated on the basis of potential flow theory the value of R_{eff} is questionable.

The results for the right-angled and the round model show that for a smoothly varying glottis model the so-called vena contracta effect does not appear (Pelorson 1994). This effect is an additional pressure loss due to sharp edges at the upstream side of a constriction.

The flow visualizations show that the vortex structure is symmetric which in the case of the round glottis model means that the Coanda effect has not yet established itself in the short time of the experiment. So a model of the glottis must not incorporate the Coanda effect if the unsteadiness of the flow is large enough. A comparison of the simulation with the visualizations shows that the potential flow model captures the overall features

of the jet formation. The appearance of instabilities in the global vortex structure, however, is not yet accurately described.

References

[Ba] Bachelor, G. H., An Introduction to Fluid Dynamics. Cambridge University Press, 1976

[Bi] Birkhoff G. Helmholtz and Taylor instability. Proc. Symp. Appl. Math. 1962.

[BM] Beale, J.T. Majda, A. High order accuracy vortex methods with explicit velocity kernels. J. Comp. Phys. 1985 **88**, 188-220.

[CB] Chorin, A.J. Bernard, P.S. Discretisation of a vortex sheet, with an example of roll-up. 1973 J. Comp. Phys. **13**, 423-429

[GR] Gradjan, Rayzik Tables of Sums and Integrals.

[HVDHW] G. Hofmans, E.A.I. van de Ven, J. den Doelder, A. Hirscberg and A.P.J. Wijnands Unsteady flow through 2-D chanels with a constriction. Preprint

[K1] Krasny, R. A study of singularity formation in a vortex sheet by the point vortex method. 1986 J. Fluid. Mech. **167**, 65-93.

[K2] Krasny, R. Desingularisation of periodic vortex sheet roll-up. 1986 J. Comp. Phys. **65**, 292-313.

[Ku] Kundu P.K Fluid Mechanics.

[L] Leonard A. Vortex methods for flow simulation. 1980 J. Comp. Phys. **37**, 289-335.

[P] Petters, M.C.A.M. Aeroacoustic sources in internal flows. Ph.D. Thesis. Eindhoven University of Technology.